Title

Conserved basal lamina proteins, laminin and nidogen, are repurposed to organize mechanosensory complexes responsible for touch sensation.

Authors

Alakananda Das[1], Joy A. Franco[2,†], Lingxin Wang[1,†], Dail Chapman[1,†], Lucy M. Wang[2], Chandni Jaisinghani[1], Beth L. Pruitt[3], Miriam B. Goodman[1*]

[1] Department of Molecular and Cellular Physiology, Stanford University, Stanford, CA 94305

[2] Department of Mechanical Engineering, Stanford University, Stanford, CA 94305

[3] Departments of Mechanical Engineering and Molecular, Cellular, & Developmental Biology, University of California Santa Barbara, Santa Barbara, CA

*Correspondence: mbgoodmn@stanford.edu

†Current addresses

Joy A. Franco, Department of Neurobiology, Harvard Medical School, Boston, MA 02115

Dail Chapman, Department of Biology, Georgetown University, Washington, DC 20057

Lingxin Wang, Novel Human Genetics Research Unit, GSK, Collegeville, PA 19426

Summary

The sense of touch is conferred by the conjoint function of somatosensory neurons and skin cells. These cells meet across a gap filled by a basal lamina, an ancient structure found in all metazoans. Using *Caenorhabditis elegans* nematodes, we show that mechanosensory complexes essential for touch sensation reside at this interface and contain laminin, nidogen, and the MEC-4 mechano-electrical transduction channel proteins. These proteins fail to coalesce into discrete, stable structures in dissociated neurons and in touch-insensitive *mec-1*, *mec-9* and *mec-5* secreted ECM protein mutants. MEC-4, but not laminin or nidogen, is destabilized in animals where somatosensory neurons secrete MEC-1 carrying missense mutations in the C-terminal Kunitz domain. Thus, neuron-epithelial cell interfaces are instrumental in mechanosensory complex assembly and function. Drawing on computational modeling, we propose that these complexes concentrate mechanical stress into discrete foci and they enhance touch sensitivity. Consistent with this idea, loss of nidogen reduces the density of mechanoreceptor complexes, the amplitude of the touch-evoked currents they carry, and touch sensitivity in parallel. These findings imply that somatosensory neurons secrete

proteins that actively repurpose the basal lamina to generate special-purpose mechanosensory complexes responsible for vibrotactile sensing.

Keywords

Basal lamina, neuron, mechanoelectrical transduction channels, mechanosensation, touch

Introduction

Touch is our most intimate sense. It is initiated by mechanical deformation of the skin generated by direct application of static force or mechanical vibration. Among other adaptive behaviors, vibrotactile sensation enables animal communication, mate-finding, and mating (Hill, 2008). Additionally, touch sensation is instrumental for the proper cognitive and emotional development of humans and other primates (Cascio et al., 2019). In all animals, vibrotactile sensing is made possible by somatosensory neurons that innervate and integrate into the animal's skin and these neurons all use ion channels to convert physical deformation into electrical signals. Many vibrotactile sensory neurons are closely opposed to epidermal cells or to specialized, epidermal-derived sensory cells, while some appear to weave paths among cells in the epidermis (Han et al., 2012; Jiang et al., 2019; O'Brien et al., 2012; Talagas et al., 2020; Yin et al., 2021). Lining the epidermis is a basement membrane or basal lamina (BL), a ubiquitous and conserved extracellular matrix (ECM) that surrounds tissues in all metazoans (Aumailley, 2021). Whereas the instructive role that the BL microenvironment plays in patterning somatosensory neurons within the skin is well-characterized (Yin et al., 2021), its contribution to the molecular events responsible for touch sensation remains to be fully elucidated.

Basal lamina are thin (ca. 100 nm), mechano-signaling biomaterials that are evolutionarily ancient and contain a core set of proteins that are conserved in all metazoans: laminin, collagen type IV, nidogen, and heparan sulfate proteoglycans or HSPS (Hynes, 2012). Laminin is a heterotrimeric protein composed of laminin-α, laminin-β and laminin-γ subunits that typically assemble into continuous sheets anchored to the cell surface by a triple helical coiled-coil stalk and globular domains that bind membrane protein receptors. Nidogen links laminin, collagen, and the heparan sulfate proteoglycan, perlecan, in BL and other ECMs (Aumailley et al., 1993). Humans and other mammals have at least 16 distinct laminin heterotrimers (Aumailley, 2013). Conservation among vertebrate laminin isoforms and antibody cross-reactivity complicates efforts to determine which isoforms are present in specific tissues, including the skin and peripheral nervous system (Domogatskaya et al., 2012). *C. elegans*

nematodes, by contrast, have only two laminin isoforms with distinct tissue localization and functions in organogenesis (Huang et al., 2003). They contain one of two laminin-α proteins (EPI-1, LAM-3), a single laminin-β (LAM-1) protein, and a single laminin-γ (LAM-2). *C. elegans* express several conserved laminin-binding proteins such as nidogen (NID-1), perlecan (UNC-52), syndecan (SDN-1), dystroglycan (DGN-1), and fibulin (FBL-1) (Keeley et al., 2020). These conserved BL proteins all contribute to the organization of neuromuscular junctions and the proper alignment of presynaptic structures with postsynaptic receptors across animal taxa [reviewed in (Sanes and Lichtman, 1999)], but their role in somatosensory function is less well understood.

Apart from the mechanoelectrical transduction (MeT) channels themselves, many other proteins affect mechanosensation either directly by contributing to force transfer from the skin to the channels, or indirectly by modulating cell stiffness and morphology, protein trafficking, and channel positioning. Genetic approaches in *C. elegans* have identified more than a dozen proteins specifically required for touch sensation (Chalfie and Sulston, 1981; Chalfie and Au, 1989), including *mec-4* which encodes an essential pore-forming subunit of the MeT required for touch sensation (O'Hagan et al., 2005) and *mec-5, mec-1,* and *mec-9* that encode ECM proteins (Du et al., 1996; Emtage et al., 2004). With the exception of *mec-5,* all of the genes linked specifically to touch sensation are expressed by the somatosensory touch receptor neurons or TRNs (Ernstrom and Chalfie, 2003). Defects in *mec-5*, *mec-1*, and *mec-9*, disrupt MEC-4 channel positioning (Du et al., 1996; Emtage et al., 2004) but have little, if any effect on how force applied to the skin is converted into longitudinal strain in the touch receptor neurons (Nekimken et al., 2020).

Here, we leverage new molecular tools for visualizing the well-characterized MEC-4 channel (Katta et al., 2019) and BL proteins (Keeley et al., 2020) to investigate the molecular basis of channel positioning in vibrotactile sensory neurons. Our approach combines genetic dissection with static and dynamic imaging in living animals and cultured sensory neurons, fluorescence recovery after photobleaching (FRAP), and *in vivo* electrophysiology. Although some MEC-4 puncta co-localize with RAB-3 in mobile synaptic vesicles, the majority are discrete stationary and stable clusters that co-localize with similarly stable and discrete BL puncta containing laminin and nidogen. Loss of NID-1 nidogen reduces laminin and MEC-4 puncta density as well as mechanoreceptor current amplitude, confirming that nidogen contributes to the organization and function of channel-ECM complexes *in vivo*. Three ECM genes previously linked to touch sensation, *mec-5*, *mec-1*, and *mec-9* (Du et al., 1996; Emtage

et al., 2004), are required for the proper subcellular organization of both the keystone ion channel, MEC-4, and the nidogen and laminin-containing BL anchor. The large MEC-1 protein, which is expressed by the TRNs and presumed to localize to the ECM, is seen to play a dual role, with its C-terminal Kunitz domain being required to integrate MEC-4 channels into the membrane-ECM spanning mechanosensory complex. The picture that emerges from these findings is that somatosensory neurons actively repurpose conserved BL proteins to form a mechanosensory complex that bridges the neuronal plasma membrane to the extracellular matrix and is instrumental in converting touch-inducted longitudinal strain into electrical signals.

Results

Recent advances in genome editing using CRISPR/Cas9 enable engineering endogenous genetic loci in *C. elegans* to encode fusions between the encoded protein and bright, stable fluorescent proteins such as mNeonGreen (mNG) and wrmScarlet (wSc) (Heppert et al., 2016; Hostettler et al., 2017; El Mouridi et al., 2017). This approach minimizes disruption to genetic regulatory elements and maximizes the ability to determine the subcellular localization of the tagged proteins. We started with a suite of transgenic *C. elegans* strains expressing mNG fusions of BL proteins and their putative transmembrane receptors (Keeley et al., 2020) and built a set of dual-color transgenic strains that enabled us to visualize the BL structures at the interface between the TRNs and the ensheathing epithelial cells and their alignment with MeT channels *in vivo* and in dissociated, cultured neurons.

ECM proteins laminin and nidogen are present in a punctate distribution along TRNs

To better understand the extracellular matrix proteins affecting touch sensation and influencing the distribution of MEC-4 channels along TRNs, we performed a screen to identify other ECM proteins that constitute the ECM around TRNs. We analyzed 30 *C. elegans* strains expressing fluorescent protein-labeled core basement membrane proteins or their putative transmembrane receptors under endogenous *cis* regulatory control at their native locus (28 strains) or within a synthetic, single copy locus (2 strains), and looked for their localization along the TRNs. These transgenic alleles represent 27 conserved BL proteins and their putative membrane receptors (Table S1). For two main reasons, we focused this analysis on the ALM neurons: 1) no other neurons are nearby and 2) the ALM cell bodies and axons are separated from the body wall muscles and other tissues known to express core basement membrane proteins. We found 12 of 27 proteins along the ALM neurites either in a uniform or punctate distribution (Figure 1). Nine appeared to be uniformly distributed along ALM: FBL-1 fibulin, MIG-6 papilin, UNC-52 perlecan, HIM-4 hemicentin, SAX-7 L1CAM, SDN-1 syndecan, PAT-2 α-integrin, EPI-1 laminin-α and LET-805 myotactin (Figure 1A). All of these proteins are also associated with other tissues such as the animal's feeding organ (pharynx), body wall muscle, and somatic gonad (Clay and Sherwood, 2015). These observations identify two new constituents of the mechanosensory ECM (papilin, perlecan, and EPI-1 laminin-α) and reinforce prior work showing that overexpressed fusions of GFP to HIM-4 hemicentin (Vogel and Hedgecock, 2001), FIB-1 fibulin (Muriel et al., 2005), SDN-1 syndecan (Rhiner et al., 2005), SAX-7 L1-CAM (Díaz-Balzac et al., 2016) and endogenously-tagged LET-805 myotactin

(Coakley et al., 2020) associate with the TRNs. Their presence in the TRN-associated ECM suggests that proper touch sensation depends on conserved molecular constituents of the ECM skin-neuron interface.

Three ancient and core basal lamina proteins localized to puncta distributed along TRNs: LAM-1 laminin-β, LAM-2 laminin-γ and NID-1 nidogen (Figure 1B). *C. elegans* has two laminin-α proteins, LAM-3 and EPI-1. Although very faint EPI-1::mNG fluorescence was detected uniformly along the ALM (Figure 1A) and LAM-3 was not detected along the TRNs, neither laminin-α subunit was observed in puncta along any of the TRNs. Because the appearance of laminin-β, laminin-γ and nidogen along the TRNs was similar to that found previously for MEC-4 (Árnadóttir et al., 2011; Chelur et al., 2002; Chen and Chalfie, 2015; Cueva et al., 2007; Emtage et al., 2004; Katta et al., 2019; Petzold et al., 2013; Vásquez et al., 2014), we measured inter-punctum intervals for TRN-associated laminin and nidogen puncta and compared them to those found for mNG::MEC-4, which was expressed from the single-copy *pgSi116* transgene. Although the distribution of interpunctum intervals of LAM-1, LAM-2, and NID-1 were more similar to one another than to mNG::MEC-4 (Table 1), which has shorter inter-punctum intervals on average, the general distribution of all four proteins was comparable (Figure 1C). Discrete laminin and nidogen puncta were not obviously associated with other neurons or with other tissues such as the pharynx and gonad, where these proteins appear to uniformly coat tissues in continuous sheets, or the in the body wall muscles in which they appear as stripes (Huang et al., 2003; Keeley et al., 2020). Collectively, these findings strongly imply that the ancient and conserved BL proteins, laminin and nidogen, are organized in a tissue-specific manner and suggest that they are reorganized and repurposed to form a specialized and discrete puncta in the BL adhered to mechanosensory TRNs.

Laminin, Nidogen and MEC-4 co-localize to complexes that decorate TRNs

Based on the similar distribution of LAM-1, LAM-2, NID-1 puncta, and MEC-4 channel proteins in the TRNs (Figure 1B,C), we hypothesized that laminin and nidogen co-assemble with MEC-4 channels *in vivo*. We developed dual-color transgenic animals expressing mNG and wSc-tagged protein pairs to investigate this question in detail. Laminin and nidogen puncta strongly co-localize with each other and with MEC-4 puncta (Figure 2A). To quantify co-localization of protein pairs, we developed custom code (Methods) to compute the intensity correlation quotient or ICQ, a method that relies upon co-variation in fluorescence intensity as a metric of colocalization (Li et al., 2004). For reference and as a positive control, we computed

ICQ in animals co-expressing mNG- and wSc-tagged NID-1. Consistent with the expectation that laminin and nidogen co-assemble into a single complex, ICQ values for LAM-1/LAM-2 and NID-1/LAM-2 pairs were similar to those measured for the NID-1/NID-1 pair (Figure 2B, Table 1). The LAM-1/MEC-4 and NID-1/MEC-4 pairs (Figure 2B, Table 1) also resulted in high ICQ values, indicating strong co-localization. Because the small size of TRN neurites (200-300 nm in diameter) might yield spurious evidence of colocalization, we also determined ICQ values for a pair of proteins that differ in their distribution with the ALM neurites. For this purpose we chose PAT-2 and MEC-4. Both are membrane proteins expressed by the touch receptor neurons (TRNs) (Chen and Chalfie, 2014; Driscoll and Chalfie, 1991; Taylor et al., 2021) that differ in their appearance in the ALM neurons: PAT-2 α-integrin has a uniform appearance and MEC-4 localizes to discrete puncta (Figure 1A, 1B). As expected for proteins that do not co-localize to common structures but are present in the same diffraction-limited volume, the PAT-2/MEC-4 pair yields ICQ values close to zero (Figure 2B, Table 1). From these observations, we conclude that MEC-4, laminin, and nidogen, co-assemble to form specialized and discrete mechanosensory complexes responsible for touch sensation and that these structures are not co-assembled with integrins.

Next, we sought to determine the mobility and stability of mechanosensory complexes using time-lapse imaging and fluorescence recovery after photobleaching (FRAP). In time-lapse images, represented as kymographs in Figure 2C, we observed that mNeonGreen-tagged MEC-4, LAM-2 and NID-1 puncta are immobile over a time course of several minutes. While photobleached MEC-4 puncta recovered to only about 25% of initial fluorescence levels, LAM-2 and NID-1 puncta did not recover any detectable fluorescence 5 minutes after photobleaching (Figure 2C). The limited mobility of laminin and nidogen observed in mechanosensory complexes is not a general property of these proteins, since laminin and nidogen recover nearly 10 and 20%, respectively, of their fluorescence 5 minutes after photobleaching in other tissues (Keeley et al., 2020). Moreover, the failure to recover fluorescence after photobleaching is not a general property of proteins associated with the ALM neurite. SDN-1 syndecan, a transmembrane heparan sulfate proteoglycan that uniformly coats the ALM (Figure 1A), recovered ~75% of its baseline fluorescence in the same time frame (Figure 2C, far right). Our observations also cannot be due to a general lack of fluidity or mobility in the TRN plasma membrane, since myristoylated-GFP expressed in the TRNs recovers half of its fluorescence within only 1 minute after bleaching (Figure S1). Thus, myristoylated-GFP and SDN-1::mNG, but not mNG::MEC-4 molecules in puncta are freely diffusible in the plasma membrane. Together,

these findings establish that MEC-4, laminin, and nidogen co-localize to mechanosensory complexes that are stationary and stably anchored in place within the TRN neurites.

MEC-4 released from mechanosensory complexes redistributes into a diffuse membrane pool

The stable incorporation of laminin, nidogen, and MEC-4 into mechanosensory complexes and prior evidence that loss of *mec-1, mec-5,* or *mec-9* function disrupts MEC-4 puncta (Emtage et al., 2004) suggested to us that laminin and nidogen puncta might also depend on *mec-1, mec-5*, and *mec-9* expression. To test this idea, we analyzed mechanosensory complex structures in *mec-5(u444), mec-1(e1496), mec-1(e1738)* and *mec-9(u437)* null mutants using NID-1 and MEC-4 as a proxies for the matrix and membrane-associated parts of the mechanosensory complex, respectively. NID-1::wSc puncta were not detected along any of the mutant ALM neurons, which were visualized by expression of a cytoplasmic GFP marker (Figure 3A). Similar results were obtained using LAM-2::mNG (Figure S2A). mNG::MEC-4 puncta were also mostly absent in these mutants with the exception of a few occasional bright punctate structures (Figure 3B). Thus, formation, assembly, and positioning of both MEC-4 channels and their associated laminin-nidogen BL structures depends on expression of *mec-1, mec-5*, and *mec-9*. The two alleles of *mec-1* we analyzed, *e1496* and *e1738*, were previously identified as null alleles that differ in an attachment phenotype (Emtage et al., 2004). In *e1496* mutants, the ALM fails to separate from body wall muscles and lies adjacent to body wall muscles in adult animals (and are considered detached), while in *e1738* mutants the ALM neurons are found in their wild-type position in adults. We confirm this attachment phenotype in our imaging and find that NID-1 puncta were affected to similar extents in these mutants (Figure 3A). Thus, the contribution of *mec-1* to organizing mechanosensory complexes is genetically distinct from its role in positioning the TRNs in the body. The role of *mec-1, mec-5,* and *mec-9* in sculpting the core components of the ECM appears to be specific to the TRNs, since the association of laminin and nidogen with other tissues, such as the gonad (Figure S2B-C) was grossly normal. Collectively, these findings indicate that MEC-1, MEC-5, and MEC-9 are needed to form, organize, or to stabilize MEC-4 channels and BL structures within mechanosensory complexes in *C. elegans* TRNs.

Since the ECM around TRNs *in vivo* is constituted from proteins secreted both by the TRNs and the surrounding epidermal cell, we next examined the distribution of MEC-4 protein in cultured TRNs, where the TRNs are isolated from the epidermal cells. To reach this goal, we

applied methods for dissociating *C. elegans* embryos and maintaining their cells in culture to transgenic animals expressing mNG::MEC-4 in the TRNs (Methods). A subset of embryonic cells in such cultures are known to express TRN-specific genes (Zhang et al., 2002) and to display TRN-like morphologies (Christensen et al., 2002; Lockhead et al., 2016; Zhang et al., 2002; Zheng et al., 2015). A majority of these TRN neurons adopt an ALM-like fate in culture (Lockhead et al., 2016; Zheng et al., 2015), providing a useful comparison to our *in vivo* studies. Despite the preservation of gene expression and general morphology, the neurites emanating from TRN cell bodies in culture are curved and often branch in ways that are rarely, if ever seen in wild-type animals *in vivo* (Figure 3C, left). We asked if TRNs cultured on thin stripes of adhesive proteins might better reproduce the *in vivo* morphology consisting of straight, unbranched neurites. To do this, we used photopatterning techniques (Strale et al., 2016) to create arrays of thin stripes of peanut lectin agglutinin (PNA) on glass coverslips. As shown in Figure 3C, TRNs grown on PNA stripes, but not on uniform PNA coatings extend straight neurites as they do *in vivo*. Given that isolated and cultured TRNs are separated from their native, structured ECM *in vitro*, this observation suggests that PNA stripes can substitute for the native ECM in constraining TRN morphology. TRNs cultured on PNA stripes had neurites that were 51.9±17.3 μm long (mean±s.e.m., n = 76 neurites, range: 24.7-102.4μm) after 24 hours and 55.5±24.5μm (mean±s.e.m., n =35, range: 30.0-122.1 μm) after 48 hours. These values are similar to those reported previously from cells cultured on coverslips uniformly coated with PNA and labeled with GFP in the cytoplasm [50.8±2.5μm, n=170 neurites, range: 8.0-183.0μm; data credit — (Lockhead et al., 2016)]. Thus, thin PNA stripes constrain neurite shape, but not overall length.

In cultured TRNs, mNG::MEC-4 was visible mainly as diffuse fluorescence, and this diffuse signal was adequate to visualize the TRN neurites. However, we also observed some punctate mNG::MEC-4 structures in the cultured TRN neurites. These puncta often exhibited bidirectional movement with frequent pauses and reversals, reminiscent of vesicles transporting cargo. To test this idea, we examined MEC-4 puncta in dual-color transgenic strains that carried the synaptic vesicle marker mCherry::RAB-3 in the TRNs. While in control animals *in vivo*, only 8.7% of mNG::MEC-4 puncta co-localized with mCherry::RAB-3, 69% and 72% of the mNG::MEC-4 puncta in *mec-1(e1738)* and *mec-9(u437)* mutant animals, respectively, co-localized with mCherry::RAB-3 (Figure 3D, S3A-C). Similarly, 55% of mNG::MEC-4 puncta in cultured TRNs also co-localized with mCherry::RAB-3 (Figure 3D, S3D). This suggests that most of the punctate mNG::MEC-4 structures seen in *mec-5*, *mec-1*, *mec-9* animals *in vivo* and

in cultured TRNs *in vitro* represent MEC-4 in vesicles and not MEC-4 in mechanosensory complexes. The size of the MEC-4 vesicular pool is small relative to the total MEC-4 fluorescence (less than 10% on average) and is insensitive to the presence or absence of sensory complexes, as the proportion of MEC-4 fluorescence that co-localize with RAB-3 vesicles does not differ significantly between control, *mec-1(e1738)* or *mec-9(u437)* mutants *in vivo* or in cultured TRNs *in vitro* (Figure 3E). Using time-lapse imaging, we found that most, if not all, mobile MEC-4 puncta co-localized with mobile RAB-3 puncta both *in vivo* and *in vitro* (Figure 3F,G), but never co-localized with NID-1::wSc puncta *in vivo* (Figure S3E). These results further support their vesicular nature and distinguish them from immobile plasma membrane mechanosensory complexes.

Because a similar pattern of MEC-4 protein distribution was evident in *mec-5, mec-1*, and *mec-9* null mutant TRNs *in vivo* and in cultured TRNs *in vitro*, we propose that MEC-4 normally exists in at least two pools in the neurite membrane: one punctate and one diffuse. Further, we propose that connection to organized BL structures is required to establish or maintain the punctate pool. In other words, MEC-4 molecules redistribute from the punctate to the diffuse pool in absence of organized BL structures. The simplest version of this model makes three predictions: 1) total MEC-4 fluorescence in ALM neurites is similar with or without organized BL structures; 2) fluorescence intensity of the diffuse MEC-4 pool is higher in neurites without organized BL structures; 3) MEC-4 protein in the diffuse pool is more mobile compared to MEC-4 protein within mechanosensory puncta.

We tested each of these predictions in turn, focusing on *mec-1(e1738)* and *mec-9(u437)* mutant alleles because the ALM neurites in these alleles are morphologically similar to wild-type. We found that the amount of MEC-4 protein present in the diffuse pool increased in *mec-1(e1738)* and *mec-9(u437)* mutants (Figure 3H, Table 1), despite the fact that there is less total mNG::MEC-4 protein in the mutant ALM neurites. The proportion of mNG::MEC-4 associated with the punctate and diffuse pools is similar in *mec-1(e1738)* and *mec-9(u437)* mutant ALM neurites *in vivo* (Figure 3I, left) and control neurons cultured *in vitro* (Figure 3I right, Table 1). Thus, whether they are disrupted by gene mutations *in vivo* or by physical separation in culture, the loss of discrete mechanosensory complexes in the TRNs redirects MEC-4 protein into a diffuse plasma membrane pool. Finally, we sought to test the prediction that MEC-4 molecules in the diffuse plasma membrane pool have increased mobility by measuring the fractional recovery of diffuse mNG::MEC-4 fluorescence intensity after photobleaching (FRAP) in control and mutant ALM neurites *in vivo*. On average, both mutants showed higher fractional

fluorescence recovery 5 minutes after photobleaching compared to control (Figure 3J,K). The mean fractional recovery after 5 minutes for diffuse mNG::MEC-4 fluorescence in *mec-1(e1738)* and *mec-9(u437)* animals was (mean±sd) 0.39±0.23 and 0.34±0.17, respectively, compared to 0.25±0.13 for punctate mNG::MEC-4 in WT animals. Thus, two of the three predictions noted above are well-supported by our experimental findings. The decrease in total MEC-4 protein present in *mec-1* and *mec-9* neurites could reflect defects in MEC-4 biosynthesis, stability, or an increase in recycling of destabilized mechanosensory complexes. Further studies will be needed to differentiate among these possibilities.

Thus, an intact mechanosensory BL governs the proportion of MEC-4 proteins that localize to discrete, stationary puncta in the plasma membrane *vs.* being diffused in the plasma membrane, reduced the total amount of protein in the axons, but does not affect the proportion of MEC-4 protein that is sequestered in RAB-3 vesicles *in vivo*. Collectively, these findings imply that MEC-4 is directed into diffuse membrane pools in the absence of a properly structured BL. This analysis is an early step toward reconstructing the biosynthesis of mechanosensory puncta and the role RAB-3+ vesicles play in the subcellular distribution of mechanosensory channels in sensory neurons *in vitro* and *in vitro*.

Mechanosensory complexes assembly depends on nidogen and laminin, but not MEC-4

Having established that MEC-4, laminin, and nidogen co-localize to stable, stationary complexes in the ALM neurons, we next used genetic dissection to learn more about how these complexes are assembled. Focusing on the genes encoding MEC-4, laminin, and nidogen, we first measured laminin and nidogen puncta in *mec-4* null mutants. LAM-2 and NID-1 puncta were unaffected by loss of *mec-4* function (Figure 4A-C, Table 1), indicating that although MEC-4 is an essential pore-forming subunit of the MeT channel in the TRNs (O'Hagan et al., 2005), it is not needed to form ECM puncta along TRN neurons. Thus, MEC-4 does not, by itself, nucleate sensory complexes in mechanosensory neurons.

Next, we sought to determine whether or not laminin and nidogen were essential to form mechanosensory complexes and to position MEC-4 channels. Because early loss of any of the four *C. elegans* laminin genes, *epi-1, lam-3, lam-1,* and *lam-2,* causes lethality in embryos or larvae (Kao et al., 2006), we could not analyze mechanosensory puncta in laminin null mutant adults. We could, however, analyze the small number of *epi-1(gm57)* mutants that survive to adulthood (Forrester et al., 1998) and *lam-3(ok2030)* mutant L1 larvae derived from a parental strain carrying a balancer chromosome. Given that laminin-α is essential for laminin trimer

assembly (Kao et al., 2006; Yurchenco et al., 1997), investigating MEC-4 channel position in *epi-1* and *lam-3* laminin-α mutants provides insight on the role that laminin trimers play in organizing mechanosensory puncta. In *epi-1(gm57)* mutants that survive to adulthood, the ALM cell bodies and sensory neurites displayed ectopic branching and multiple segments were seen adjacent to the body wall muscle, displaced from their control position (Figure 4D, Table 1). TRN neurite segments that were adjacent to the body wall muscle in *epi-1(gm57)* mutants displayed only diffuse mNG::MEC-4 fluorescence. By contrast, segments that retained their wild-type position retained discrete MEC-4 puncta with IPIs indistinguishable from control animals (Figure 4E-F). Thus, wild-type EPI-1 laminin-α is required to position the ALM neurons in the worm's body, but dispensable for positioning mechanosensory complexes along properly attached ALM neurons. Next, we analyzed MEC-4 puncta in control L1 larvae and in *lam-3(ok2030)* mutants. As in adults, MEC-4 localized to discrete puncta in control L1 larvae (Figure 4G-J). In *lam-3(ok2030)* larvae, by contrast, MEC-4 puncta were either undetectable or when visible (Figure 4G), they were fewer in number and more widely separated. The increase in mean and median IPI values (Table 1) we found in *lam-3(ok2030)* larvae is likely to underestimate the effect of *lam-3* loss-of-function, however, since in several ALMs mNG::MEC-4 signal could not be visualized distinctly and were thus not analyzed. Thus, wild-type EPI-1 adheres to TRNs (Figure 1A) and is needed to maintain proper ensheathment within epidermal cells and LAM-3 is needed for mechanosensory complex assembly. Thus, the two *C. elegans* laminins proteins play distinct, but overlapping roles in mechanosensation, as they do in embryonic development (Huang et al., 2003).

Like laminin, nidogen is a core BL protein that is conserved in all vertebrates and invertebrates (Mayer et al., 1998). Unlike laminin, nidogen is not needed for BL assembly (Ackley et al., 2003; Bader et al., 2005; Böse et al., 2006; Dai et al., 2018; Dong et al., 2002; Kang and Kramer, 2000; Kim and Wadsworth, 2000, Murshed et al., 2000; Schymeinsky et al., 2002; Wolfstetter et al., 2019) and nidogen null mutants develop into grossly normal adult animals. MEC-4 channel puncta were dimmer and spaced further apart in *nid-1* mutants compared to control animals and the remaining puncta retained their alignment with NID-1 (Figure 5A-D, Table 1). The decrease in mechanosensory complex density was accompanied by an increase in the proportion of MEC-4 protein present in the diffuse membrane pool. This redistribution of MEC-4 protein occurred without any noticeable change in the total mNG::MEC-4 fluorescence (Figure 5E, Table 1). Consistent with these observations, ICQ values for NID-/MEC-4 pairs were reduced in *nid-1* mutants compared to control animals, but higher

than expected for uncorrelated proteins (Figure 5F, Table 1). Collectively, these findings reinforce the idea that MEC-4 channels redistribute to a diffuse membrane pool following perturbations of mechanosensory complexes and that BL play an instructive role in the assembly or stability of sensory complexes. They also imply that touch sensation and mechanotransduction should be impaired, but not absent in *nid-1* mutants.

We tested this prediction using classical behavioral assays and by recording mechanoreceptor currents (MRCs) from ALM neurons. We found that *nid-1(cg119)* null mutants are slightly less touch-sensitive than wild-type animals and more sensitive than *mec-4* null mutants (Figure 5G), suggesting that the sensory complexes visible in this mutant retained their function in mechanotransduction. To learn more, we directly recorded MRCs in control and *nid-1* mutant mutants. To optimize our ability to detect a partial loss-of-function, we used an ultrafast mechanical stimulator that evokes currents that are approximately five-fold larger than those evoked by slower stimuli (Katta et al., 2019). Using this approach, we found that MRCs were qualitatively similar in *nid-1* mutants and wild-type controls (Figure 5H), but that MRCs were smaller in *nid-1* mutants (Figure 5I). Such a decrease in MRC amplitude is the predicted effect of the observed increase in the interpunctum interval or IPI (Katta et al., 2019). The effect of *nid-1* on TRN membrane current is specific to MRCs, since voltage-gated currents were similar to wild-type controls in all respects (Figure S4). Thus, we conclude that the impaired touch sensation found in *nid-1* mutants arises from the decreased density of sensory complexes. The mild phenotype observed in the absence of nidogen might point to redundancy with another laminin linker protein.

Nidogen inclusion in mechanosensory complexes is independent of laminin binding

Which nidogen domains help to position mechanosensory complexes along TRN neurites? Wild-type, full-length NID-1 protein contains three conserved globular domains, G1, G2 and G3 (Figure 6A). The N-terminal G1 and G2 domains are connected by a flexible linker, whereas the G2 and G3 domains are connected by a more rigid rod-like domain consisting of a series of EGF motifs (Fox et al., 1991; Patel et al., 2014). The *nid-1(cg118)* allele, which was isolated in a transposon-mediated genetic screen (Kang and Kramer, 2000), encodes a large in-frame deletion of G1, G2 and part of the first EGF motif of the rod domain (Figure 6A). In *nid-1(cg118)* mutants, MEC-4 puncta distributions were similar to wild-type (Figure 6C-E top, Table 1). Thus, neither the G1 nor the G2 domains of nidogen are required to assemble or position mechanosensory complexes. The G1 and G2 domains of nidogen are likewise

dispensable for expression of NID-1 protein during embryonic development and in BL associated with muscles, the somatic gonad, and neuronal tracts (Kang and Kramer, 2000).

Next, we examined the role of the G3 domain thought to bind to laminin-ɣ (Aumailley et al., 1993; Fox et al., 1991; Mann et al., 1988, 1989; Mayer et al., 1998; Patel et al., 2014; Takagi et al., 2003) by using CRISPR mediated genome editing to create a NID-1[ΔG3] mutant (*pg146)*. Like *nid-1(cg119)* null mutants (Ackley et al., 2003; Kang and Kramer, 2000), the *nid-1(pg146)* mutants developed into grossly wild-type adult animals. Also similar to *nid-1(cg119)*, MEC-4 puncta were dimmer and spaced further apart in *nid-1(pg146)* mutants (Figure 6C-E middle, Table 1). Thus, NID-1 G3 domain is required for MEC-4 puncta distribution. Given that the *pg146* NID-1[ΔG3] mutant phenocopies the *nid-1(cg119)* null allele with respect to MEC-4 puncta distribution, we determined whether or not this is due to the inability of the truncated NID-1[ΔG3] protein to incorporate into mechanosensory complexes by visualizing a wSc-tagged NID-1[ΔG3] isoform. Consistent with the idea that the laminin-γ-binding G3 domain is required to incorporate NID-1 into BL, NID-1[ΔG3]::wSc was absent from the BL around the pharynx, body wall muscle and gonad, in contrast to full length NID-1. However, NID-1[ΔG3]::wSc was visible in neuronal-associated BL, including the nerve ring and in puncta along ALM neurons (Figure S5B). These findings imply that the nidogen G3 domain is required to incorporate nidogen into conventional BL and that it acts in parallel with another factor to support inclusion in mechanosensory complexes and other neuronal BL.

The nidogen G3 domain has been shown to form strong binding interactions with laminin-ɣ (Aumailley et al., 1993; Fox et al., 1991; Mann et al., 1988, 1989; Mayer et al., 1998; Patel et al., 2014; Takagi et al., 2003). To learn more about the role of the nidogen G3 domain in mechanosensory complexes, we sought to disrupt the nidogen-laminin binding interface by engineering mutations in laminin. To reach this goal, we leveraged biochemical and structural studies identifying three residues in a conserved loop within an EGF motif of laminin-γ as crucial for laminin-nidogen binding (Poschl et al., 1994; Pöschl et al., 1996; Takagi et al., 2003). These residues are an aspartate and an asparagine, which are conserved in *C. elegans* LAM-2 laminin-γ (D840, N842) and a valine, which corresponds to an isoleucine in LAM-2 (I844) (Figure 6B). We edited the endogenous *lam-2* locus to encode a LAM-2[D840N, N842S, I844S] triple mutant isoform, which we refer to as LAM-2[NSS]. We chose these particular substitutions because they had the largest fold-change in binding affinity between mammalian nidogen and laminin-γ short arm fragments *in vitro* (Mayer et al., 1998; Pöschl et al., 1996). Unlike *lam-2* null mutants, LAM-2[NSS] mutant animals were viable with no apparent defects in gross morphology

or development. As expected for loss of nidogen-laminin binding, NID-1::wSc fluorescence was severely reduced in the BL lining the pharynx and body wall muscle in LAM-2[NSS] mutants (Figure S5C). Despite these dramatic effects in conventional basal lamina, LAM-2[NSS] mutants appeared to retain NID-1 in the nerve ring (Figure S5C) and also retained a wild-type distribution of MEC-4 (Figure 6C-E bottom, Table 1). Collectively, these findings suggest that LAM-2 acts in parallel with another binding partner to incorporate NID-1 into neuronal BL, including the specialized mechanosensory complexes in the TRNs, but not in other tissues. Additional studies will be required to identify these other factors.

MEC-1 connects the MEC-4 channel to ECM components of the sensory complex

The *mec-1* gene is predicted to encode a large protein containing fifteen Kunitz (Ku) domains [see (Emtage et al., 2004) and Figure 7A], which are commonly characterized as protease inhibitors but are also found in peptide toxins that bind to ion channels (Mishra, 2020). Several toxins in this family bind to and affect the function of ASIC channels (Cristofori-Armstrong and Rash, 2017), raising the possibility that toxins mimic endogenous Ku domain proteins that bind to the extracellular domains of DEG/ENaC/ASIC channels. MEC-1 Ku15 shares 33% sequence identity with the snake neurotoxin MitTx-alpha (Baconguis et al., 2014) (Figure 7B). We investigated this idea *in vivo*, leveraging known and new missense mutations affecting MEC-1 Ku15. The *e1526* and *u811* alleles lead to the expression of full-length MEC-1[R1804C] and MEC-1[C1808Y], respectively. Unlike the residue affected in *e1526* allele, the one affected in *u811* is conserved and predicted to form a disulfide bond likely to be integral to folding Ku15 (Figure 7B). *mec-1(e1526)* and *mec-1(u811)* animals are known to be touch insensitive (Emtage et al., 2004), but how these mutations affect all elements of mechanosensory complexes is not known. Using CRISPR/Cas9 genome editing, we mutated C1808 of Ku15 either to a serine (encoded by the *pg154* allele) to prevent disulfide bond formation while preserving the size of the amino acid side chain and to tyrosine (encoded by the *pg164* allele), to recreate the *u811* mutation. We used dual-color transgenic animals expressing NID-1::wSc and mNG::MEC-4 and found that all of these *mec-1* alleles retained nidogen puncta but very few mNG::MEC-4 puncta (Figure 7C-E). NID-1 puncta were distributed in a manner nearly indistinguishable from control animals in MEC-1[R1804C] mutants (Figure 7C-E, top row), while NID-1 puncta were denser in the two alleles affecting C1808 (Figure 7C-E middle and bottom row, Table 1). Laminin puncta were also retained in the MEC-1[R1804C] mutant animals and co-localized with nidogen (Figure S6). Collectively, these results demonstrate that

an intact Ku15 is needed to link MEC-4 to BL structures. Additional support for this conclusion comes from the findings that, in all of these *mec-1* missense alleles, the bulk of mNG::MEC-4 fluorescence shifts to the diffuse pool (Figure 7F, Table 1), ICQ values for MEC-4/NID-1 are reduced by half (Figure 7G, Table 1), and animals are strongly touch-insensitive (Figure 7H). Based on these perturbations in Ku15 and their distinct effects on MEC-4, laminin, and nidogen puncta, it is tempting to propose that MEC-1 physically binds to MEC-4 through Ku15.

Mechanosensory complexes bridging the neuron-matrix interface could concentrate mechanical stress

The mechanosensory complexes tether the plasma membrane of the TRNs to foci in the extracellular matrix. We investigated the potential mechanical implications of an array of such protein tethers using a finite-element modeling (FEM) approach. Specifically, we simulated the response of a neurite to mechanical stimulation in the presence and absence of protein tethers. In this reduced system, the neurite is modeled as a hemi-cylinder with uniform material properties that do not change in the vicinity of mechanosensory complexes. The model reproduced the general shape of the TRNs seen *in vivo* and the influence of tethers was generated by linking a 1-μm long domain to a reference point at each punctum. Given that MEC-4 channels are mostly likely to be activated by tangential forces (Sanzeni et al., 2019), we modeled touch-induced forces as tangential forces applied at the reference point. The effect of this tangential force is distributed among the linked nodes with nodes at the center of the region experiencing a larger force and nodes at the edge of the region experiencing a smaller force. The size of the tangential force is determined by the average shear strain over the puncta that results from the touch stimulation. This shear strain is multiplied by a constant representing the stiffness of the tether. Since tether stiffness is not known, we picked a value that produced realistic tether forces in the piconewton range. Simulations with and without these tangential forces represent neurites with and without protein tethers. Neurites that lack synthetic simulated tethers (represented by focal tangential forces) have a uniform strain energy density distribution, while neurites with synthetic tethers display regions of higher strain energy density (Figure 8A). These results suggest tethers amplify the mechanical signal that results from touch stimulation and that perturbations that affect their density, material properties, or the mechanical properties of the lipid bilayer itself are all expected to modulate touch sensitivity.

Discussion

Given the intimate association between the TRNs and epidermal cells, we reasoned that elements of the *C. elegans* matrisome might help to position the MEC-4 channels in the TRNs. The *C. elegans* matrisome includes a core set of proteins that is ancient and conserved across metazoans (Clay and Sherwood, 2015; Kramer, 2003). Leveraging a suite of transgenic animals expressing mNeonGreen-fusion proteins from their native loci (Table S1), we show that a subset of these proteins adhere to the TRNs, including laminin (LAM-1, LAM-2, EPI-1), nidogen (NID-1), perlecan (UNC-52), hemicentin (HIM-4), syndecan (SDN-1) and fibulin (FBL-1). Among these, only laminin and nidogen assume a punctate distribution reminiscent of the distribution of MEC-4 in the TRNs. Drawing upon still- and live-imaging of MEC-4 channels and matrisome proteins tagged alone and in pairs, FRAP, and genetic dissection, we show that MEC-4, laminin, and nidogen co-localize to previously unknown mechanosensory complexes that link the membrane to the matrix and are both stationary and remarkably stable.

These focal complexes have theoretical implications for how mechanical stress is distributed along the longitudinal axis of the TRNs during touch. Specifically, finite-element modeling shows that mechanical stress is elevated in the vicinity of complexes relative to the flanking areas of the plasma membrane (Figure 8). These features match those expected for a MeT channel that operates according to a force-from-filament (FFF) model *in situ* (Anishkin and Kung, 2013; Katta et al., 2015; Kung, 2005). The large (~1 μm) size of the visible laminin-nidogen structures drives us to speculate that they also underpin the non-linear viscoelastic mechanics needed to account for the bidirectional activation of MRCs and for their frequency-dependence (Eastwood et al., 2015; Katta et al., 2019; Sanzeni et al., 2019). Collectively, these experimental findings and our prior computational analyses strongly support a model in which: (1) the MEC-4 MeT is activated via a FFF model; and (2) the laminin-nidogen structures function as extracellular filaments essential for vibrotactile sensing *in vivo*.

Given that ensheathment of somatosensory neurons by epidermal cells is shared by other animals (Yin et al., 2021), including humans (Talagas et al., 2020), and that laminin-dependent filaments have been reported in murine somatosensory neurons (Chiang et al., 2011), these findings open the door to the idea that BL proteins are repurposed to form force-transmitting filaments in sensory neurons. Although a detailed view of how mechanosensory complexes form requires further study, this work provides several key entry points that support an initial model for how these mechanosensory complexes assemble and function (Figure 8B). First, laminin-nidogen puncta form in the absence of MEC-4 channels but

MEC-4 puncta are sparse in mutants carrying defects in the *lam-3* laminin-alpha and *nid-1* nidogen genes. Because *nid-1* mutants have mild impairments in behavioral and electrical responses to touch, the complexes that are present in these mutants are competent to function as MeT channels. Second, we infer that the sensory neurons actively direct the assembly of mechanosensory complexes, through proteins like MEC-1 and MEC-9 which are secreted by the TRNs. Specifically, *mec-1* and *mec-9* null mutants fail to form aligned stable complexes containing MEC-4, laminin, and nidogen (Figure 3). The mild phenotype of *nid-1* mutants may point to redundancy with another factor that is assembled in a *mec-1* or *mec-9*-dependent manner. Third, MEC-1 harbors specific domains required for co-assembly and alignment of MEC-4, laminin and nidogen. In particular, mutations predicted to disrupt folding of the c-terminal Kunitz domain in MEC-1 leave laminin and nidogen ECM structures intact but disrupt localization of MEC-4 to discrete puncta (Figure 7).

Whereas MEC-4 localizes primarily to stationary mechanosensory complexes in wild-type and fully touch-sensitive animals, MEC-4 redistributes almost exclusively to a diffuse membrane pool in *mec-1(e1738)* and *mec-9(u437)* mutants lacking discernable organized BL structures. A similar situation is also evident in cultured TRNs that are physically separated from epidermal cells and their native BL structures. The few MEC-4 puncta that are present in these conditions represent MEC-4 molecules that are sequestered in RAB-3-positive vesicles (Figure 3). Given that *mec-1(e1738)* and *mec-9(u437)* mutants are completely touch insensitive (Du et al., 1996; Emtage et al., 2004), the MEC-4 proteins present in the diffuse membrane pool are not capable of supporting mechanosensation. Similarly, no *mec-4*-dependent mechanically-activated currents are seen in cultured TRNs (Sangaletti et al., 2014; Suzuki et al., 2003). Since cultured TRNs appear to maintain their cell-autonomous gene expression profiles (Lockhead et al., 2016; Zhang et al., 2002), their voltage-activated currents (Christensen and Strange, 2001; Suzuki et al., 2003), and their shape [this study and (Christensen and Strange, 2001; Christensen et al., 2002; Lockhead et al., 2016; Zhang et al., 2002)], the failure to form mechanosensory puncta most likely arises from the physical separation from epidermal tissues and the subsequent disruption in the organization of laminin and nidogen along TRNs. Given that somatosensory neurons are ensheathed by epidermal cells in other animals, including mammals, the failure to maintain the *in vivo* organization of mechanoelectrical transduction channels *in vitro* may have broad implications for studies of dissociated and cultured sensory neurons.

Wherever neurons meet skin or muscle cells, the gap between them is occupied by a basal lamina, containing ancient and conserved proteins like laminin and nidogen. The BL is an active molecular medium, as evidenced by the fact that laminin plays an instructive role in organizing ion channels at the neuromuscular junction (Rogers and Nishimune, 2017). Laminin also governs the mechanosensitivity of cultured mouse dorsal root ganglion neurons (Chiang et al., 2011). In this study, we identified laminin and its binding partner, nidogen, as essential partners for organizing and positioning of the mechanoelectrical transduction channel, MEC-4, along *C. elegans* TRNs. This finding extends the concept that the BL is an active medium from motor neurons to sensory neurons and defines mechanosensory complexes as multiprotein complexes linking neurons to the BL matrix.

Acknowledgements

We thank Tom Clandinin and Ellen Kuhl for comments and advice, the entire WormsenseLab for feedback on experimental and analytical design, Zhiwen Liao for technical support and worm injections, and WormBase for supporting experimental design. We thank Martin Chalfie, Kang Shen, and the Caenorhabditis genetics center (supported by the NIH Office of Research Infrastructure, P40 OD010440) for *C. elegans* strains. We are especially grateful to David Sherwood for sharing key transgenic strains prior to publication. Confocal fluorescence imaging used instruments in the Stanford University Cell Sciences Imaging Core Facility (RRID:SCR_017787) and protein patterning used instruments in the Stanford Nanofabrication Facility (supported by NSF Award ECCS-2026822). Research funded by NIH grant R35105092 to MBG, F99NS115219 fellowship to JAF, F32NS116193 fellowship to DC, and a BioX interdisciplinary fellowship to LMW.

Author contributions

Conceptualization, A.D., J.F., D.C., B.L.P., M.B.G.;
Methodology, A.D., J.F.;
Software, A.D., J.F., L.W., L.M.W.;
Validation, A.D., J.F., L.W.;
Formal analysis, A.D., J.F., L.W., L.M.W;
Investigation, A.D., J.F., L.W., D.C., L.M.W., C.J.;
Resources, A.D., J.F., L.W., B.L.P., M.B.G.;
Data Curation, A.D., J.F., L.W.;
Writing - Original draft, A.D., J.F., L.W., D.C.;
Writing - Review and editing, A.D., J.F., L.W., D.C., M.B.G.;
Visualization, A.D., J.F., L.W., L.M.W.;
Supervision, A.D., M.B.G.;
Project administration, A.D., M.B.G.;
Funding acquisition, M.B.G.

Declaration of Interests

The authors declare no competing interests.

Figure Legends

Figure 1. Screening 27 basal lamina (BL) proteins and their receptors reveals nine proteins that uniformly coat TRNs neurites and three that appear as discrete puncta similar to MEC-4 mechanically-gated ion channels.

A. Nine BL proteins uniformly coat TRN neurites *in vivo.* Representative fluorescence confocal micrographs of adult TRNs in transgenic animals expressing BL proteins visualized using CRISPR/Cas9 to insert mNeonGreen (mNG) or GFP (SAX-7, LET-805) into native loci. Panels show ALM neurons coated with BL proteins, oriented as shown in the upper left panel (clockwise from the upper left): FBL-1 fibulin, UNC-52 perlecan, MIG-6 papilin, HIM-4 hemicentin, EPI-1 laminin-α, PAT-2 α-integrin, LET-805 fibronectin, SAX-7 L1 CAM, SDN-1 syndecan. Scale bar: 10 μm. See Table S1 for a full list of all strains used in this experiment.

B. Three BL proteins localize to discrete puncta along TRN neurites. Fluorescence widefield micrographs showing LAM-1::wSc laminin-β, LAM-2::mNG laminin-ɣ, NID-1::wSc nidogen localizing to discrete puncta distributed along the ALM neurons, similar to mNG::MEC-4 (bottom). Scale bar: 10 μm.

C. Raincloud plots of the distribution of interpunctum intervals (IPI) for each protein shown in panel B. Each raincloud shows a probability distribution of IPIs (top) and the individual IPIs (bottom). Black circles denote mean, boxes denote the median and the interquartile ranges of the population. Summary statistics are collected in Table 1A.

Figure 2. Nidogen, laminin, and MEC-4 co-assemble into stationary, stable mechanosensory complexes.

A. Pairwise colocalization of NID-1, LAM-2, LAM-1, and MEC-4 tagged with wormScarlet (magenta) and mNeonGreen (green). Representative fluorescence micrographs of ALM neurites in double-labeled strains. Reference condition for high colocalization: punctate NID-1 is tagged with two fluorophores (NID-1::wSc, NID-1::mNG) (upper left). Reference condition for low colocalization: uniform PAT-2::wSc and punctate mNG::MEC-4 (lower right). Scale bar: 10 μm.

B. Intensity correlation quotient (ICQ) for protein pairs in panel A. Values close to 0.5 indicate maximal intensity correlation and co-localization, values close to 0 indicate no correlation, and values close to -0.5 indicate anticorrelation. Each green circle shows a measurement from a single ALM neurite. White circles show the mean and the vertical black bars show standard

deviation. Summary statistics are collected in Table 1B.

C. Representative, time-lapse imaging of (left to right) MEC-4, LAM-2, NID-1, and SDN-1 puncta. Top two panels in each column show puncta before and after bleaching, respectively; the bottom panel shows kymographs (distance-time images) of a 10 s pre-bleach period and 300 s observation period. See also Figure S1.

D. Fluorescence recovery after photobleaching (FRAP) for MEC-4, LAM-2, NID-1, and SDN-1 puncta. Recovery was minimal for MEC-4, LAM-2, and NID-1 and substantial for SDN-1 during the observation period. Dark traces show the average trajectory of fluorescence recovery; shaded regions show the standard deviations for 23, 11, 11, and 8 neurons analyzed for MEC-4, LAM-2, NID-1, and SDN-1, respectively. See also Figure S1.

Figure 3. The TRN-associated extracellular matrix is essential for stable mechanosensory complexes to form in vivo and in vitro, but not for sequestering MEC-4 into RAB-3-positive vesicles.

A-B. NID-1 and MEC-4 puncta are absent in *mec-5*, *mec-1*, and *mec-9* null mutants. Representative fluorescence micrographs of animals co-expressing NID-1::wSc and a cytoplasmic GFP marker in the TRNs (A) and in animals expressing mNG:MEC-4 (B) lack discrete NID-1 and MEC-4 puncta, respectively. Two *mec-1* alleles were analyzed: in *e1496*, the TRNs are displaced from their wild-type body position and seen adjacent to NID-1 labeling in body wall muscles and in *e1738,* the TRNs retain their wild-type position. Scale bars: 10 μm. See also Figure S2.

C. Representative images of TRNs expressing mNG::MEC-4 cultured on uniformly coated PNA coverslips (left) and on thin parallel stripes of Alexa Fluor 594 conjugated PNA (right). Green fluorescence (top) and merged red-green-brightfield images (bottom) are shown for each condition. Scale bars: 10 μm. Similar observations are found in *n*=78 and 76 independent biological replicates.

D. Proportion of mNG::MEC-4 puncta that correspond to the plasma membrane mechanosensory complexes (not co-localized with RAB-3 positive vesicles, dark green) vs. puncta that represent vesicles (co-localized with RAB-3 positive vesicles, light green) as a function of genotype *in vivo* and in cultured TRNs. For the ALMs *in vivo*, analysis was limited to a distance of 150 μm from the cell body, while the entire neurite was analyzed for TRNs *in vitro*. A total of *n*= 25, 29, 24, and 71 ALM neurites were analyzed for control, *mec-1(e1738)*, *mec-9(u437) in vivo* and TRNs *in vitro*, respectively. See also Figure S3.

E. Proportion of mNG::MEC-4 fluorescence associated with non-vesicle (dark green) and vesicle pools (light green) as a function of genotype and in cultured TRNs. Same dataset as in panel D was used for this analysis. For the ALMs *in vivo*, analysis was limited to a distance of 150 um from the cell body, while the entire neurite was analyzed for TRNs *in vitro*. Error bars are the standard deviation of a total of *n* = 25, 29, 24, and 71 ALMs analyzed for each condition.
F-G. Kymographs of dual-labeled TRNs showing that mobile mNG::MEC-4 puncta co-localize with mobile mCherry::RAB-3 puncta *in vivo* (F) and *in vitro* (G). Scale bars: 10 µm.
H. Total mNG::MEC-4 fluorescence in ALM neurites *in vivo* as a function of genotype. Stacked bars show the average fluorescence (arbitrary units) visible as puncta (dark green) and diffuse (light green) fluorescence. Error bars are the standard deviation of a total of *n* = 18, 17, and 17 ALMs. Summary statistics are collected in Table 1C.
I. Proportion of total mNG::MEC-4 fluorescence associated with punctate and diffuse pools as a function of genotype (same dataset as in panel I for *in vivo* measurements) and in cultured TRNs. Stacked bars show the percentage of total fluorescence visible as puncta (dark green) and diffuse (light green) fluorescence. Error bars are the standard deviation of a total of *n* = 18, 17, 17, and 76 ALMs analyzed for each condition. Summary statistics are collected in Table 1C.
J. Representative *in vivo* time-lapse imaging of MEC-4 puncta in (left to right): wild-type, *mec-1(e1738),* and *mec-9(u437)* animals. Top two panels in each column show puncta before and after bleaching, respectively; the bottom panel shows kymographs (distance-time images) of a 10 s pre-bleach period and 300 s observation period. Control data is replicated from Figure 2C, mNG::MEC-4.
K. Fluorescence recovery after photobleaching (FRAP) for MEC-4 in wild-type, *mec-1(e1738),* and *mec-9(u437)*. Dark traces show the average trajectory of fluorescence recovery of MEC-4 fluorescence; light traces show the results for individual trials for 22, 22, and 25 ALMs in the indicated genotypes. Recovery is accelerated for diffuse MEC-4 fluorescence in *mec-1(e1738)* and *mec-9(u437)* relative to discrete puncta in Control. Control data is replicated from Figure 2D, mNG::MEC-4.

Figure 4. ECM mechanosensory complexes can form in the absence of MEC-4, but the laminin-alpha subunit LAM-3 is needed for MEC-4 channels to assemble into mechanosensory complexes.

A. Representative images showing discrete NID-1::wSc and LAM-2::mNG puncta distributed along the ALM neurons in *mec-4(u253)* null background. Scale bars: 10 µm.

B. Raincloud plots of the distribution of interpunctum intervals (IPI) for NID-1 and LAM-2. Each raincloud shows the probability distribution of IPIs (top) and the individual IPIs (bottom). Black circles denote mean, boxes denote the median and the interquartile ranges of the population. Summary statistics are collected in Table 1A.
C. Cumulative distribution plots of the data in panel B (magenta and green lines are NID-1 and LAM-2 in *mec-4(u253)* mutants, respectively) overlaid with data in control animals for each protein (gray lines, replotted from Figure 1C).
D. Representative images showing discrete mNG::MEC-4 puncta distributed along the ALM neurons and TRN morphology defects (yellow arrows) in *epi-1(gm57)* adult animals. Scale bars: 10 μm.
E. Raincloud plots of the distribution of interpunctum intervals (IPI) for mNG::MEC-4 in *epi-1(gm57)* mutant animals. Due to the TRN morphological defects the complete TRNs could not be analyzed in their entirety; instead IPIs were measured in 13 segments that were at least 50 μm long drawn from 9 ALM neurites. The raincloud shows the probability distribution of IPIs (top) and the individual IPIs (bottom). Black circles denote mean, boxes denote the median and the interquartile ranges of the population. Summary statistics are collected in Table 1A.
F. Cumulative distribution plots of mNG::MEC-4 puncta distribution in *epi-1(gm57)* mutants and control animals. The green and gray lines are data for *epi-1(gm57)* and control, respectively. Control IPIs were computationally selected from randomly positioned 50 μm ALM segments in control animals from the dataset shown in Figure 1C to provide a better match to the analysis available for ALM segments in *epi-1(gm57)* animals.
G. Representative images showing mNG::MEC-4 puncta in control and *lam-3(ok2030)* mutant L1 larvae. White boxes indicate the area expanded in panel H. Scale bars: 50 μm.
H. Expanded view of the ALM neurons in the boxed area in panel G. Scale bars: 10 μm.
I. Raincloud plots of the distribution of interpunctum intervals (IPI) for mNG::MEC-4 in *lam-3(ok2030)* mutant L1 larvae. Each raincloud shows the probability distribution of IPIs (top) and the individual IPIs (bottom). Black circles denote mean, boxes denote the median and the interquartile ranges of the population. Summary statistics are collected in Table 1A.
J. Cumulative distribution plots of the data in panel I (green line shows MEC-4 intervals in *lam-3(ok2030)* mutant) compared to control MEC-4 IPIs in L1 larvae (gray line).

Figure 5. Nidogen is required for wild-type organization of mechanosensory complexes and for behavioral and neural responses to touch.

A-B. MEC-4 and LAM-1 puncta spread out in *nid-1* mutants. (A) Representative images of mNG::MEC-4 and LAM-1::wSc obtained from dual-color transgenic animals in a *nid-1* mutant background. Scale bars: 10µm. (B) Intensity line scans derived from images in panel A showing alignment of MEC-4 and LAM-1 peaks.

C. Raincloud plots of the distribution of interpunctum intervals (IPI) for mNG::MEC-4 (green) and LAM-1::wSc (magenta) in *nid-1(cg119)* mutant animals. Each raincloud shows the probability distribution of IPIs (top) and the individual IPIs (bottom). Black circles denote mean, boxes denote the median and the interquartile ranges of the population. Summary statistics are collected in Table 1A.

D. Cumulative probability distribution of MEC-4 (top) and LAM-1 (bottom) IPI in ALM neurites. Larger intervals dominate the distribution in *nid-1* mutants (green and magenta) compared to control (gray).

E-F. *nid-1* loss of function reduces the coupling between MEC-4 and LAM-1 and redistributes MEC-4 to a diffuse membrane pool. (E) Total mNG::MEC-4 fluorescence *in vivo* as a function of genotype. Stacked bars show the average fluorescence (arbitrary units) visible as puncta (dark green) and diffuse (light green) fluorescence. Error bars are the standard deviation of a total of *n* = 21 ALMs for each genotype. Summary statistics are collected in Table 1C. (F) Intensity correlation quotient as a function of genotype. Control data replicated from Figure 2B. Green points are measurements of individual dual-color images, White circles are mean and vertical bars represent standard deviation. Summary statistics are collected in Table 1B.

G-I. *nid-1* loss of function decreases behavioral and neural responses to touch. (G) Touch response as a function of genotype, using wild-type (N2) and *mec-4(u253)* null animals as references. Bars are the average (± SEM) response to 10 touches of *n=75* animals tested blind to genotype in 3 independent cohorts. (H) Mechanoreceptor currents (MRCs) evoked by indentation pulses of the indicated amplitude. Representative traces for control (left, gray) and for *nid-1(cg119)* (right, green) mutants are shown. Similar results obtained in 12 and 8 recordings for control and *nid-1* animals, respectively. (I) Peak MRC amplitude at the onset of stimulation as a function of stimulus displacement. Dark gray and dark green traces are the average of the lighter gray and green traces for control and *nid-1* mutants, respectively. See also Figure S4.

Figure 6. ***The G3 domain, but not the G1 and G2 domains of NID-1 nidogen are needed to position MEC-4 channels in vivo***

A. Schematic of NID-1 showing the ΔG1-G2 (*cg118*) and ΔG3 (*pg146*) in-frame deletions. Large boxes show the indicated globular domains. Small gray boxes show EGF domains.
B. (Top) Schematic of LAM-2. Large boxes show the indicated globular domains. Small gray boxes show EGF domains. (Bottom) Sequence of the EGF8 domain predicted to bind NID-1, and its sequence alignment with its counterpart in mouse laminin-γ1. The residues mutated in the *pg153* LAM-2[NSS] allele are highlighted in pink.
C-E. Mechanosensory complexes visualized by analyzing MEC-4 puncta distribution. (C) Representative images of mNG::MEC-4 puncta in (top to bottom): *cg118* NID-1[ΔG1-G2], *pg146* NID-1[ΔG3], and *pg153* LAM-2[NSS] mutant backgrounds. Scale bars: 10 μm. (D) Raincloud plots of interpunctum intervals (IPI) for mNG::MEC-4 (green) in NID-1[ΔG1-G2], NID-1[ΔG3], and LAM-2[NSS] mutant animals. Each raincloud shows the probability distribution of IPIs (top) and the individual IPIs (bottom). Black circles denote mean, boxes denote the median and the interquartile ranges of the population. (E) Plots of cumulative probability distribution of mNG::MEC-4 IPIs in the indicated alleles (green) vs control worms (gray, replotted from Figure 1C). Summary statistics are collected in Table 1A. See also Figure S5.

Figure 7. Disrupting Ku15 in full-length MEC-1 prevents proper assembly of mechanosensory complexes and causes touch-insensitivity.
A. Schematic of the longest MEC-1 isoform showing fifteen predicted Kunitz domains (brick red) and EGF repeats (gray).
B. Amino acid sequence of Ku15 compared to that of MitTx, a Kunitz domain-containing ion channel toxin (Baconguis et al., 2014) (left) and a homology model (right) of MEC-1 Ku15 based on MitTx structure (PDB ID: 4NTX).
C-E. Mechanosensory complexes visualized in dual-color transgenic animals expressing mNG::MEC-4 and NID-1::wSc in *mec-1* missense alleles affecting Ku15. Sparse MEC-4 puncta are no longer aligned with NID-1, which appears denser. (C) Dual-color fluorescence images of ALM neurons in the indicated *mec-1* alleles. Scale bars: 10 μm. Boxed area in *pg164* MEC-1[C1808Y] is shown in the expanded view below. (D) Raincloud plots of IPIs for NID-1::wSc puncta (magenta) in *e1526* MEC-1[R1804C], *pg154* MEC-1[C1808S], and *pg164* MEC-1[C1808Y] mutant animals. Each raincloud shows the probability distribution of IPIs (top) and the individual IPIs (bottom). Black circles denote mean, boxes denote the median and the interquartile ranges of the population. (E) Plots of cumulative probability distribution of

NID-1::wSc IPIs in the indicated *mec-1* alleles (magenta) vs control worms (gray). Summary statistics are collected in Table 1A. See also Figure S6.

F. MEC-4 distribution as a function of genotype for *mec-1* missense alleles. Stacked bars show the average fluorescence in the punctate (dark green) and diffuse (light green) pools and their sum is the integrated average mNG::MEC-4 fluorescence. 16, 13, 16, and 15 independent replicates analyzed for each genotype. Summary statistics are collected in Table 1C.

G. Plot of ICQ values calculating MEC-4 and NID-1 colocalization as a function of genotype. Control data replicated from Figure 2B. Individual points represent independent measurements in ALM neurites. White circles show mean and vertical black bars show the standard deviation. Summary statistics are collected in Table 1B.

H. Touch sensitivity as a function of genotype, assessed in a 10-touch assay. Bars represent the average (±SEM) of 75 animals tested in 3 independent cohorts blinded to genotype.

Figure 8. Punctate ECM tethers at mechanosensory complexes can create localized areas of high strain energy density

A. Modeling the strain energy distribution in a simulated TRN with or without discrete tethers (boxed area) connecting the TRN to the ECM, shows concentrated regions of high strain energy density (red) around the tethered region.

B. Diagram summarizing the localization, origin and inter-relationships between the MEC-4 MeT channel (green) and the ECM proteins laminin-α, laminin-β (LAM-1), laminin-γ (LAM-2), nidogen (NID-1), collagen (MEC-5) and Kunitz domain protein (MEC-1). Thick gray arrows indicate the origin of the ECM proteins. Thin dark dual ended arrows indicate putative physical interactions that are implied from previous literature or suggested by the observations in this study. The membrane and ECM components of the mechanosensory puncta are encompassed by green and magenta dotted lines, respectively.

Tables

Table 1: Summary statistics for IPI, ICQ and MEC-4 fluorescence intensity measurements

Table 1: Summary statistics for IPI, ICQ and MEC-4 fluorescence intensity measurements

A. IPI measurements

Protein	Figure #	Genotype	Mean (um)	Median (um)	Standard deviation (um)	#IPI	#ALMs
LAM-1::wSc	1C	*lam-1(pg136)/+ IV; uIs31 III*	5.33	4.28	3.88	1703	24
LAM-2::mNG	1C, 4C, S6C	*lam-2(qy20) X; uIs115*	5.68	4.54	4.34	2051	29
NID-1::wSc	1C, 4C	*nid-1(pg138) V; uIs31 III*	5.18	4.41	3.24	2057	25
mNG::MEC-4	1C, 6E	*pgSi116 II*	4	3.2	2.82	3227	31
NID-1::wSc	4B,C	*nid-1(pg138) V; uIs31 III; mec-4(u253) X*	5.14	4.03	3.95	1744	20
LAM-2::mNG	4B,C	*lam-2(qy20)mec-4(u253) X; uIs115*	5.66	4.66	4.1	1480	22
mNG::MEC-4	4E,F	*pgSi116 II; epi-1(gm57) IV*	3.64	3.01	2.47	514	9 (13 segments)
mNG::MEC-4 (simulated)	4F	*pgSi116 II*	3.94	3.2	2.57	12554	31 (1000 segments)
mNG::MEC-4 (L1)	4I,J	*pgSi116 II; lam-3(ok030) I*	2.86	2.34	2.19	566	17
mNG::MEC-4 (L1)	4J	*pgSi116 II*	2.26	2.14	1.04	1248	28
mNG::MEC-4	5C,D	*pgSi116 II; lam-1(pg136)/+ IV; nid-1(cg119) V*	7.31	5.42	6.07	1185	22
LAM-1::wSc	5C,D	*pgSi116 II; lam-1(pg136)/+ IV; nid-1(cg119) V*	6.95	5.04	5.95	1265	22
mNG::MEC-4	5D	*pgSi116 II; lam-1(pg136)/+ IV*	4.19	3.53	2.73	2041	21
LAM-1::wSc	5D	*pgSi116 II; lam-1(pg136)/+ IV*	5.15	4.28	3.5	1679	21
mNG::MEC-4	6D,E	*pgSi116 II; nid-1(cg118) V*	3.88	3.01	3.06	2424	25
mNG::MEC-4	6D,E	*pgSi116 II; nid-1(pg146) V*	8.65	6.78	7.1	1142	24
mNG::MEC-4	6D,E	*pgSi116 II; lam-2(pg153) X*	3.95	3.2	2.85	2415	24
NID-1::wSc	7E	*pgSi116 II; nid-1(pg138) V*	3.68	3.02	2.16	1835	14
NID-1::wSc	7D,E	*pgSi116 II; nid-1(pg138)mec-1(e1526) V*	3.34	2.77	1.88	2296	19
NID-1::wSc	7D,E	*pgSi116 II; nid-1(pg138)mec-1(pg154) V*	3	2.52	1.78	2096	15
NID-1::wSc	7D,E	*pgSi116 II; nid-1(pg138)mec-1(pg164) V*	2.77	2.14	2.3	1976	13
LAM-2::mNG	S6B,C	*lam-2(qy20) X; mec-1(e1526) V; uIs115*	5.11	3.78	4.61	2051	29

B. ICQ measurements

Protein pair	Figure #	Genotype	Mean	Standard deviation	#ALMs
NID-1 NID-1	2B	*nid-1(pg138)/nid-1(qy38) V*	0.39	0.015	8
NID-1 LAM-2	2B, S6E	*nid-1(pg138) V; lam-2(qy20) X*	0.27	0.032	13
LAM-1 LAM-2	2B	*lam-1(pg136)/+ IV; lam-2(qy20) X*	0.30	0.024	14
NID-1 MEC-4	2B, 7G	*nid-1(pg138) V; pgSi116 II*	0.37	0.021	14
LAM-1 MEC-4	2B, 5F	*lam-1(pg136)/+ IV; pgSi116 II*	0.29	0.035	21
PAT-2 MEC-4	2B	*pat-2(pg125) III; pgSi116 II*	0.05	0.023	15
LAM-1 MEC-4	5F	*lam-1(pg136)/+ IV; pgSi116 II; nid-1(cg119) V*	0.12	0.034	22
NID-1 MEC-4	7G	*pgSi116 II; nid-1(pg138)mec-1(e1526) V*	0.15	0.021	19
NID-1 MEC-4	7G	*pgSi116 II; nid-1(pg138)mec-1(pg154) V*	0.21	0.034	15
NID-1 MEC-4	7G	*pgSi116 II; nid-1(pg138)mec-1(pg164) V*	0.13	0.031	13
NID-1 LAM-2	S6E	*nid-1(pg138)mec-1(e1526) V; lam-2(qy20) X*	0.29	0.022	13

C. MEC-4 fluorescence intensity measurements

Protein	Figure #	Genotype	Punctate pool (mean±sd) AU	Diffuse pool (mean±sd) AU	Punctate fraction (mean±sd)	Diffuse fraction (mean±sd)	# ALMs
mNG::MEC-4	3H,I	*pgSi116 II*	20.74±3.13	15.0±2.0	57.91±3.75	42.09±3.75	18
mNG::MEC-4	3H,I	*pgSi116 II; mec-1(e1738) V*	2.76±0.87	19.66±3.06	12.17±2.5	87.83±2.5	17
mNG::MEC-4	3H,I	*pgSi116 II; mec-9(u437) V*	2.9±1.1	19.41±3.73	12.72±3.15	87.28±3.15	17
mNG::MEC-4	5E	*pgSi116 II*	19.9±4.31	15.05±3.3	56.87±3.55	43.13±3.55	21
mNG::MEC-4	5E	*pgSi116 II; nid-1(cg119) V*	10.05±1.89	23.73±6.94	30.67±6.03	69.33±6.03	21
mNG::MEC-4	7F	*pgSi116 II; nid-1(pg138) V*	17.72±1.99	11.36±2.19	61.19±3.29	38.81±3.29	16
mNG::MEC-4	7F	*pgSi116 II; nid-1(pg138)mec-1(e1526) V*	4.0±1.37	23.09±3.37	14.7±4.37	85.3±4.37	13
mNG::MEC-4	7F	*pgSi116 II; nid-1(pg138)mec-1(pg154) V*	6.52±1.51	17.7±2.64	26.64±3.63	73.36±3.63	16
mNG::MEC-4	7F	*pgSi116 II; nid-1(pg138)mec-1(pg164) V*	2.19±1.05	23.61±3.51	8.43±3.99	91.57±3.99	15

Methods

C. elegans strain construction and maintenance

A complete list of all *C. elegans* strains used in this study with their respective genotypes and provenance is available in the Key Resources Table. Animals were maintained at 20 °C on NGM agar plates seeded with *E. coli* OP50 unless otherwise mentioned.

We used CRISPR/Cas9-directed gene editing to insert fluorescent protein-encoding DNA at endogenous loci, or as single-copy insertion of synthetic genes at MosSCI insertion sites. Unless indicated otherwise, we relied on homologous recombination via the self-excising cassette (SEC) method (Dickinson et al., 2015). For each strain, we injected a mixture of Cas9-sgRNA plasmids (50 ng/µL), repair template plasmid (50 ng/µL), plasmids encoding visible markers [pCFJ104 (myo3p::mCherry), 5 ng/µL; pCFJ90 (myo-2p::mCherry), 2.5 ng/µL] into the gonads of 40-60 young adult wild-type (N2, Bristol) animals. Each of these individual animals was allowed to lay eggs for 2-3 days at 25°C, in the absence of selection. To select for animals carrying edits, hygromycin (500 µL, 5 mg/mL) was added to each plates and allowed to grow at 25°C for an additional 4-5 days. Candidate transgenic animals survived hygromycin treatment, red fluorescent extrachromosomal array markers, and displayed a Rol phenotype dominant roller due to the insertion of the SEC carrying the *sqt-1(e1350)* mutations. To remove the SEC, we heat-shocked plates containing ~6 L4 rollers (37°C, 75 minutes) and allowed the resulting animals to grow at 20 °C for 3-4 days. Adult NonRol animals (worms that lost both copies of the SEC) were singled and successful genome editing was verified by visualizing fluorescence and by PCR genotyping. For all strains carrying wSc-tagged LAM-1 laminin-β, we maintained and imaged animals heterozygous for the wSc-tagged *lam-1* allele with one untagged copy of *lam-1,* since homozygous wSc-tagged *lam-1* animals were sterile and exhibited several morphological defects (Keeley et al., 2020).

To generate *C. elegans* strains carrying genetic deletions or point mutations in endogenous *nid-1*, *lam-2* or *mec-1* loci, we applied the co-CRISPR method (Paix et al., 2015), using *dpy-10(cn64)* as the co-CRISPR target. All reagents were purchased from IDT Technologies: Cas9 protein (Alt-R® S.p. Cas9 Nuclease V3, 100 µg, Catalog # 1081058), tracrRNA (Alt-R® CRISPR-Cas9 tracrRNA, 5 nmol, Catalog # 1072532), crRNA for each loci (Alt-R® CRISPR-Cas9 crRNA, 2 nmol), single stranded oligomeric DNA repair templates (Ultramer™ DNA Oligonucleotides). We prepared injection mixes with equimolar amounts of tracrRNA, crRNA and Cas9 nuclease, such that the final concentration of each was 1.5 µM. If

multiple crRNAs were used for a single target site, the amounts were adjusted such that the total crRNA concentration was 1.5 μM. The *dpy-10* crRNA was used at a molar of ratio 1:14 to the target crRNAs. In the first step, we allowed the tracrRNA and crRNAs to anneal at 95°C for 5 min, followed by incubation at room temperature for 5 min. Next, we added the annealed RNA mixture to Cas9 and incubated this solution at 37 °C for 10 min. Finally, ssDNA repair template was added to generate a final concentration of 0.5μM and the total volume was adjusted to 20μL using sterile water. For each gene editing round, we injected 15-20 young adult N2 animals and then transferred individual animals to growth plates for 3-4 days at room temperature. Plates that contained many Rol progeny as evidence of successful editing were selected for further analysis. Specifically, we isolated single Rol animals and allowed them to lay eggs for 2 days (room temperature), after which the roller animals were screened for the desired mutation using PCR. Non-roller animals from the positive plates were then isolated and screened in the same way. The desired loci were sequenced in candidate lines to confirm the presence of the desired mutation.

Embryonic cell dissociation and culture

We generated cultures of mixed embryonic cells following previous methods (Bianchi and Driscoll, 2006; Sangaletti and Bianchi, 2013; Strange et al., 2007) with modifications that improved yield. We first grew animals on OP50-seeded NGM plates until they developed into gravid adults. Next, we harvested embryos from these animals using standard hypochlorite bleaching methods (Stiernagle, 2006) and allowed the resulting embryos to grow on 10 cm enriched peptone plates seeded with NA22 *E. coli*. The process of age-synchronization and growth on NA22-seeded plates was repeated for two additional cycles. Next, we separated adults from bacteria through several centrifugation and washing cycles and treated them with a sodium hypochlorite solution (6% bleach, 150 mM NaOH) to harvest embryos. The resulting embryos were rinsed three times with pH-adjusted 1x egg buffer (25 mM HEPES pH 7.3, 118 mM NaCl, 48 mM KCl, 2 mM $CaCl_2$, 2 mM $MgCl_2$, with a osmolality of 340 ± 5 mOsm) and then separated from lytic fragments using a 60% sucrose gradient. Following these steps, we incubated embryos in chitinase (25 U/mL) while rocking until ~80% of eggshells had been digested (~50 min), an endpoint that we confirmed visually. Finally, we rinsed dissociated embryos and dissociated them mechanically by trituration first through a sterile 21-gauge needle and then through a sterile 25-gauge needle. We used a 5 μm filter to remove debris from the resulting cell suspension, rinsed in buffer, and resuspended cells in sterile L-15 cell culture

media without HEPES or phenol red (Gibco™, Catalog# 21083027), seeded onto glass coverslips either coated uniformly with peanut lectin or bearing micropatterns of peanut lectin. All procedures were carried out using sterile technique on a standard benchtop and cultures were incubated in a benchtop chamber at room atmosphere and temperature (22-24°C).

Protein patterning coverslips for cell cultures

We used open-source graphic design software (Inkscape) to design custom patterns consisting of thin (8-pixels or 2.2 µm) stripes on 1824x1140 pixel canvas size. We fabricated custom reagent basins from PDMS sheets using a consumer-grade computerized die-cutting machine (Silhouette, Cameo, https://www.silhouetteamerica.com/featured-product/cameo). Stripe width and spacing was optimized to enable touch receptor neurons to generate straight neurites that were confined to lateral strips and did not traverse areas lacking peanut lectin, as described (Franco, 2021). We used these resources together with a device designed for light-activated molecular adsorption (LIMAP; Primo, Alvéole, Stanford Nanofabrication Facility) to create the desired micropatterns of peanut lectin (Unconjugated lectin from Arachis hypogea, Millipore Sigma, Catalog# L0881, Lectin PNA From *Arachis hypogaea* (peanut), Alexa Fluor™ 594 Conjugate, Invitrogen™, Catalog# L32459) on class coverslips. We adapted the general approach from Strale, et al. (Strale et al., 2016), as follows. For convenience and simplicity of coverslip handling, we used glass-bottom six-well tissue culture-grade microtiter plates (6 Micro-well glass bottom plate with 20 mm micro-well #1.5 cover glass, Cellvis ™, Catalog# P06-20-1.5-N) for cell culture experiments involving patterned coverslips. First, we plasma-treated the plates with ionized atmospheric gas for 1 minute (25 forward, zero reflected power, Plasmatech P-50, Stanford Nanofabrication Facility). Next, we positioned a PDMS reagent basin in each well, added poly-l-lysine or PLL (0.01% in sterile PBS, ~35 µl) to each well, and allowed the PLL solution to incubate for 1 hour. Following this step, we added mPEG-SVA (100 µg/mL) freshly prepared in pH-adjusted 100 mM HEPES, pH 8.0 buffer and incubated the coverslips for an additional 1 hour. Lastly, we rinsed the coverslips with distilled water and allowed them to air dry prior to the application of proprietary photoactivatable reagent, PLPP gel (Alvéole, diluted in pure ethanol at 1:6 volumetric ratio). Coverslips were allowed to air dry prior to patterning using the PRIMO system (25 ms exposure, 100% laser power, 50 mJ/mm^2 dosage), which uses light to degrade the PLPP gel according to the user-defined pattern. We transferred peanut lectin protein (PNA) to patterned coverslips in two incubation steps: 1) PBS for >5 minutes; 2) PNA (500 µg/mL) for 20 minutes. Experiments used either

simple PNA (Unconjugated lectin from Arachis hypogea, Millipore Sigma, Catalog# L0881) or PNA conjugated with AlexaFluor 594 (Lectin PNA From *Arachis hypogaea* (peanut), Alexa Fluor™ 594 Conjugate, Invitrogen™, Catalog# L32459), which enabled us to visualize the patterns. We fabricated patterns one day prior to plating dissociated embryonic *C. elegans* cells and kept them hydrated with sterile PBS until use.

Wide-field and confocal fluorescence microscopy

To visualize MEC-4 and protein constituents of the basal lamina in living animals, we used levamisole (5 mM in M9 buffer) to immobilize age-synchronized young adult worms on grooved 5% (w/v in M9 buffer) agarose pads. Grooved pads were fabricated as described (Rivera Gomez and Schvarzstein, 2018). This approach constrained animals to a straight posture along the grooves and kept animals in a common orientation: both factors enabled us to efficiently image dozens of animals in a single imaging session. We generated wide-field fluorescence images of the ALM neurites and associated BL structures using an automated inverted compound microscope equipped for epifluorescence imaging (Keyence BZ-X800). Using the instrument's stitch and align function, we first collected a low magnification image (4X) and selected individual animals to image at high magnification using either a 40X (Nikon Plan Apo, oil immersion, NA=1.0) or a 60X (Nikon Plan Apo lambda, oil immersion, NA=1.40) objective. In most cases, we used the stitch and align function to generate complete images of the ALM neurite. We kept all image acquisition parameters including exposure time, binning, camera gain settings, etc. constant for experiments comparing fluorescence intensity and/or puncta detection across several genotypes. We used the Keyence instrument to image cultured TRNs using a similar strategy, 24 or 48 hours after seeding on 6-well glass-bottom dishes coated with PNA, uniformly or in a striped pattern. We collected dual color time-lapse images for cultured TRNs at 60x (Nikon Plan Apo lambda 60x, no binning, 6 sec intervals for a total duration of 120 s), and for TRNs in vivo at 60x (Nikon Plan Apo lambda 60x, 3x3 binning, 3 sec intervals for a total duration of 120 min). For improved visualization, we generated still images of transgenic animals expressing tagged BL proteins on an inverted, laser-scanning confocal microscope (Leica SP8, Stanford Cell Sciences Imaging Facility) at 40X magnification (Leica 40X HC PL APO, CS2, oil, NA=1.30). We immobilized and mounted animals as described above.

Fluorescence recovery after photobleaching (FRAP)

We conducted FRAP experiments on an inverted, laser-scanning confocal microscope (Leica SP8, Stanford Cell Sciences Imaging Facility) at 40X magnification ((Leica 40X HC PL APO, CS2, oil, NA=1.30). Briefly, we acquired images at 1 fps for 10 frames prior to bleaching. The imaging scientist selected a region of interest (~15x15 pixels) containing a defined punctum or in an inter-punctum interval for bleaching and this region was scanned at maximum power for 3.5 s. Following bleaching, we acquired images every 5 seconds (mNG::MEC-4, LAM-2::mNG, NID-1::mNG and SDN-1::mNG) or every 1 second (myr::GFP) for 60 frames. We analyzed the resulting image stacks by tracing ALM neurites (using the segmented line tool in ImageJ), converting the image stack to a kymograph in which each time-point was represented by a straightened 21-pixel wide strip containing the ALM neurite. We inspected the kymographs for global movement of the neurite during image acquisition and for the appearance of moving puncta, excluding samples with clear evidence of movement from FRAP analysis. Once validated, we used a custom Python script (https://github.com/wormsenseLab/FRAP) to detect the bleached region based on the expectation that it would contain the maximum change in fluorescence intensity between the last three frames collected prior to bleaching and the first three frames after bleaching. The average fluorescence intensity in the bleached region for each time point was first corrected for overall photobleaching over the time period of image acquisition, by dividing by the average fluorescence intensity in the non-bleached region at the same time point. These corrected values were then normalized by setting the average pre-bleach intensity to 1 and the intensity of the first frame after photobleaching to zero.

Puncta analysis

Using images showing the entire ALM neurite generated using the stitch-and-align function of the Keyence microscope, we built an efficient image processing pipeline for analyzing puncta distribution. We traced ALM neurites as a segmented line (line parameters: width = 20 pixels, spline fit) and converted them to straightened lines using the built-in 'Straighten' function in Fiji. Next, the images were analyzed by Python script (https://github.com/wormsenseLab/IPI), handling background subtraction and plotting fluorescence intensity along the neurite. Puncta were detected from these plots using 'find_peaks' (scipy). Inter-punctum intervals were plotted as raincloud plots using the ‘ptitprince’ Python package (Allen et al., 2021).

Colocalization analysis

To assess co-localization of pairs of mNeonGreen and wormScarlet labeled proteins along the ALM neurite, we leveraged the software-control system on the Keyence BZ-X800 to collect overlapping, dual-channel images at 60x (Nikon Plan Apo, NA = $) and to stitch them together. We traced the ALM neurites in the stitched images using segmented line function (line parameters: width = 20 pixels, spline fit) and line straightening tools in Fiji. We analyzed the resulting straightened images using a custom Python image-analysis script (https://github.com/wormsenseLab/ICQ), which extracted the fluorescence intensity values for each channel along the neuron after background subtraction. Intensity correlation quotient (ICQ) is defined as the ratio of the number of pixels where the product of difference from mean for the red and green channels are positive, to the total number of pixels subtracted by 0.5 (Li et al., 2004). As a consequence, the ICQ values vary from 0.5 (perfect co-localization) to -0.5 (perfect exclusion). Dual-color labeling that is uncorrelated or whose analysis is impeded by background noise will give a value close to zero. To validate this approach to colocalization in the ALM neurons, we generated reference conditions in which near-perfect co-localization was expected (e.g. dual-labeling of NID-1 with mNG and wSc) and in which no colocalization was expected (e.g. dual-labeling with a punctate and diffuse marker). We have previously used this approach to analyze colocalization of antibody-labeled MEC-4, MEC-2 and MEC-5 in fixed TRNs, using two antibodies directed against MEC-2 as a co-localization reference (Cueva et al., 2007).

To analyze co-localization of MEC-4::mNG and mCherry::RAB-3, we collected multichannel images (Keyence BZ-X800, 60x objective, 2x2 binning for *in vivo* and 1x1 binning for *in vitro* images) and pre-processed them as described above. Puncta in both the green and red channels were identified in the straightened images by a custom Python script (https://github.com/wormsenseLab/MEC-4_RAB-3_vesicle_colocalization). For ALMs in vivo, we focused this analysis on a 150 μm-long segment of the ALM neurite immediately anterior to the cell body. For cultured TRNs, the entire neurite was analyzed. Puncta in both channels were classified as co-localized if the peaks of their intensities were located less than 0.5 μm away from each other.

MEC-4 intensity measurements and MEC-4 redistribution analysis

For measuring mNG::MEC-4 intensity along ALM neurites, overlapping images were acquired automatically on the Keyence BZ-X800 inverted epifluorescence microscope (60x objective, no binning, 1 s exposure) and seamlessly stitched together using the Keyence

proprietary image stitching software. In the stitched images ALM neurites were traced as a segmented line (line parameters: width = 20 pixels, spline fit) and straightened using the built-in 'Straighten' function in ImageJ. These straightened images were read by a custom Python script (https://github.com/wormsenseLab/MEC-4_punctate_diffuse_pools), which extracted the fluorescence intensity values along the neuron after background subtraction. The punctate and diffuse fluorescence fractions were calculated from these intensity profiles.

C. elegans touch assay

We measured touch responses using a ten-touch assay. Specifically, we delivered mechanical stimuli to age-synchronized, well-fed young adult animals with an eyebrow hair glued to a toothpick touching animals alternately in anterior and posterior regions of the body for a total of 10 times. Animals were scored as responding if they reversed direction following each stimulation. This method delivers supra-threshold stimuli, independent of experimenter or the specific eye-brow hair used (Nekimken et al., 2017). Thus, this classical method can detect decreased, but not increased sensitivity. We performed touch assays in groups of 4-5 strains, including wild-type (N2) and TU253 *mec-4(u253)* null mutants as touch-sensitive and touch-insensitive (Mec) reference conditions. Animals were tested blind to genotype in cohorts of 25 animals. At least three independent cohorts were tested for each genotype or condition.

Whole-cell patch clamp electrophysiology

We recorded from the ALM neurons in TU2769 *uIs31 [mec-17p::GFP]* and GN932 *uIs31 III; nid-1(cg119) V* following established procedures (Eastwood et al., 2015; Katta et al., 2019; O'Hagan et al., 2005). As a consequence of geometric constraints imposed by our stimulator system, most of our recordings are from the ALMR neuron. The ALMR and ALML neurons are bilaterally symmetric and exhibit no detectable differences in voltage- or touch-evoked currents (not shown). We used the following salines in all recordings. Extracellular saline contained (in mM): NaCl (145), KCl (5), $MgCl_2$ (5), $CaCl_2$ (1), and Na-HEPES (10), adjusted to a pH of 7.2 with NaOH. We added D-glucose (final concentration of 20mM) to external saline, bringing the osmolarity to ~325 mOsm. Intracellular recording solution contained (in mM): K-gluconate (125), KCl (18), NaCl (4), $MgCl_2$ (1), $CaCl_2$ (0.6), K-HEPES (10), and K_2EGTA (10), and adjusted to a pH of 7.2 with KOH. We used sulforhodamine 101 (1mM, Invitrogen) to visualize whether or not the whole-cell configuration was achieved in each recording. We used an EPC-10 USB amplifier controlled by Patchmaster software (version 2x90; HEKA/Harvard Biosciences) to record

membrane current, deliver voltage-clamp stimuli, and to control the mechanical stimulator. Mechanical stimuli were delivered using an open-loop system adapted from (Peng and Ricci, 2016) and described previously (Katta et al, 2019). Analog data (membrane potential, membrane current) were filtered at 2.9 kHz and digitized at 5 kHz.

Voltage-activated currents were measured in response to 100ms pulses between -80 and 80mV (in 20mV increments) from a holding potential of -60mV. We applied each voltage protocol in triplicate and averaged the resulting membrane current traces to improve the signal to noise, as described [Goodman et al, 1998]. Membrane voltage was corrected for errors due to liquid-junction potentials (-14 mV) and residual series resistance measured in each recording. We omitted recordings with series resistance larger than 200 MΩ and holding current more than -10 pA at -60 mV. MRCs were evoked by indentation steps (300 ms) with an interstimulus interval of 1s from a holding potential of -60mV, as described by Katta et al., 2019. We applied 3 repetitions of mechanical stimuli and averaged the resulting MRC traces. We used peak-finding software to measure peak MRC currents at the onset and offset of the mechanical stimulation pulse. For clarity, only the 'on' MRCs are shown in this study.

Homology modeling

We generated the homology model for MEC-1 15th Kunitz domain using the Phyre2 protein fold recognition server (Protein Homology/analogY Recognition Engine V 2.0) (Mezulis et al., 2015), using the structure of the neurotoxin MitTx-alpha in complex with chicken ASIC1 ion channel (PDB ID: 4NTX) (Baconguis et al., 2014). The model was rendered for publication using the The PyMOL Molecular Graphics System, Version 2.5.1 Schrödinger, LLC.

Modeling strain energy density

To investigate the potential mechanical implications of a protein tether, we developed a finite element model to simulate the response of a neurite to touch stimulation both with and without tethers. Numerical simulations were performed in Abaqus/Standard. The neurite was modeled as a 250 nm diameter semicylinder (Cueva et al., 2007) with symmetry boundary conditions to reduce computational cost. The semicylinder was discretized using 8-node linear brick elements with reduced integration and hourglass control, and a mesh convergence analysis was performed to find the appropriate element size. Material properties were uniform throughout the neurite (Young's modulus of 6.3 kPa (Krieg et al., 2017)) with no change in stiffness at the puncta. To model the deformation due to touch stimulation, we prescribed a

varying displacement of $y = e^{-5000z^2}$ along the bottom edge of the neurite to reproduce the profile shape seen in the figures in Sanzeni et al. 2019. Next, to model the influence of protein tethers, we linked a 1 μm long region of nodes to a reference point at each punctum, and an inter-punctum interval of 3 μm was used (Cueva et al., 2007) to separate neighboring puncta. At each punctum, a tangential force was applied at the reference point, and its influence was distributed among the linked nodes with the force magnitudes being largest at the center of the linked region and decreasing quadratically toward the region boundaries. The magnitude of the tangential forces was determined by the average shear strain over the linked region. This average shear strain was multiplied by a constant value representing the stiffness of the tether. Since this stiffness is not known, we picked a value of 1 mN/m (Powers et al., 2012) that produced tether forces of reasonable magnitudes in the piconewton range. Simulations with and without these tangential forces represent neurites with and without protein tethers.

Supplementary information titles and legends

Table S1. List of all strains used in screening for localization of proteins along TRNs

Figure S1. Myristoylated GFP is highly mobile in the ALM neurite plasma membrane, related to Figure 2.

A. Representative, *in vivo* time-lapse imaging of myristoylated GFP (myr::GFP) expressed in the TRNs. Top two panels in each column show fluorescence before and after bleaching, respectively; the bottom panel shows kymograph (distance-time image) of a 10 s pre-bleach period and 60 s observation period.

B. Fluorescence recovery after photobleaching (FRAP) for myr::GFP. About 70% fluorescence recovery for myr::GFP was seen during the observation period. Dark trace and shaded regions show the average and standard deviation of the trajectory of fluorescence recovery for 14 neurons.

Figure S2. LAM-2::mNG puncta along TRNs are absent in mec-1, mec-5 and mec-9 null animals, related to Figure 3.

A. Fluorescence photomicrographs of animals co-expressing LAM-2::mNG and a cytoplasmic RFP marker in the TRNs (A) showing lack of discrete LAM-2 puncta in *mec-5(u444)*, *mec-1(e1496)*, *mec-1(e1738)* and *mec-9(u437)* animals. Two *mec-1* alleles were analyzed: in *e1496*, the TRNs are displaced from their wild-type body position and seen adjacent to LAM-2 labeling in body wall muscles and in *e1738,* the TRNs retain their wild-type position. Scale bars = 10 um.

B. Fluorescence photomicrographs of animals expressing LAM-2::mNG in control, *mec-5(u444)*, *mec-1(e1496)*, *mec-1(e1738)* and *mec-9(u437)* animals showing no significant differences in LAM-2::mNG distribution in basal lamina surrounding the gonad. Scale bars: 100 um.

C. Fluorescence photomicrographs of animals expressing NID-1::wSc in control, *mec-5(u444)*, *mec-1(e1496)*, *mec-1(e1738)* and *mec-9(u437)* animals showing no significant differences in NID-1::wSc distribution in basal lamina surrounding the gonad. Scale bars: 100 um.

Figure S3. Most mNG::MEC-4 puncta in mec-1 and mec-9 null animals and in TRNs cultured in vitro co-localize with vesicle marker mCherry::RAB-3, related to Figure 3.

A-D. Fluorescent photomicrographs showing mNG::MEC-4 (green) and mCherry::RAB-3 (magenta) in control (A), *mec-1(e1738)* (B) and *mec-9(u437)* (C) animals *in vivo* and control TRNs *in vitro*. Scale bars: 10 um.

E. Kymograph of dual-labeled TRNs showing that mobile mNG::MEC-4 puncta do not co-localize with NID-1::wSc puncta *in vivo*. Scale bars: 10 µm.

Figure S4. Voltage-activated membrane current in control and nid-1 mutant ALM neurons, related to Figure 5.

A. Representative membrane current traces evoked by voltage pulses (from -80 to +80mV, in 20 mV increments) applied from a holding potential of -60 mV. Each trace represents the average of three stimulus presentations for control (left, gray) and *nid-1(cg119)* (right, green) mutants. Traces are shaded according to the voltage applied during the step. Similar results obtained in a total of 9 and 7 recordings for control and *nid-1(cg119)* animals, respectively.

B. Peak current vs. voltage. Dark gray and dark green traces are the average peak current of the lighter gray and green traces for control and *nid-1(cg119)* mutants, respectively. For individual recordings, membrane voltage is corrected for residual series resistance.

Figure S5. NID-1[ΔG3] and LAM-2[NSS] mutations disrupt nidogen/laminin binding, related to Figure 6.

A-C. Representative images showing localization of nidogen to BL surrounding the pharynx (left, white arrowhead), nerve ring (left, yellow arrow), body wall muscles (BWM) (right, white arrowhead) and ALM (right, yellow arrow) in control (A, full genotype: *nid-1(pg138) V; lam-2(qy20) X*), NID-1[ΔG3] (B, full genotype: *nid-1(pg147pg138) V; lam-2(qy20) X*) and LAM-2[NSS] (C, full genotype: *nid-1(pg138) V; lam-2(pg150qy20) X*) mutants. NID-1[ΔG3]::wSc fluorescence is not visible around the pharynx or BWM, but is present around the nerve ring and in puncta along ALM. In the LAM-2[NSS] background, NID-1::wSc fluorescence is significantly reduced around the pharynx and BWM, but is present around the nerve ring and in puncta along ALM. Scale bars: 10 um.

Figure S6. Disrupting Ku15 in full-length MEC-1 minimally affects LAM-2 puncta distribution, related to Figure 7.

A. Representative fluorescence images of LAM-2::mNG puncta in ALM neurons in *mec-1(e1526)* animals. Scale bar: 10 µm.

B. Raincloud plot of interpunctum intervals (IPI) for LAM-2::mNG puncta in *e1526* MEC-1[R1804C] mutant animals. Each raincloud shows the probability distribution of IPIs (top) and the individual IPIs (bottom). Black circles denote mean, boxes denote the median and the interquartile ranges of the population. Summary statistics are collected in Table 1A.

C. Plot of cumulative probability distribution of LAM-2::mNG IPIs in *mec-1(e1526)* (green) vs control worms (gray, data replicated from Figure 1C) showing slightly smaller IPIs in *mec-1(e1526)* animals compared to control.

D. NID-1 and LAM-2 puncta colocalize in *mec-1(e1526)* mutants. Representative images of NID-1::wSc and LAM-2::mNG obtained from dual-color transgenic animals in a *mec-1(e1526)* mutant background. Scale bars: 10μm.

E. Intensity correlation quotient as a function of genotype shows that colocalization between NID-1 and LAM-2 is unchanged between control (data replicated from Figure 2B) and *mec-1(e1526)* animals. Green points are measurements of individual dual-color images, White circles are mean and vertical bars represent standard deviation. Summary statistics are collected in Table 1B.

References

Ackley, B.D., Kang, S.H., Crew, J.R., Suh, C., Jin, Y., and Kramer, J.M. (2003). The Basement Membrane Components Nidogen and Type XVIII Collagen Regulate Organization of Neuromuscular Junctions in Caenorhabditis elegans. J. Neurosci. *23*, 3577–3587.

Anishkin, A., and Kung, C. (2013). Stiffened lipid platforms at molecular force foci. Proc. Natl. Acad. Sci. U. S. A. *110*, 4886–4892.

Árnadóttir, J., O'Hagan, R., Chen, Y., Goodman, M.B., Chalfie, M., Arnadóttir, J., O'Hagan, R., Chen, Y., Goodman, M.B., Chalfie, M., et al. (2011). The DEG/ENaC protein MEC-10 regulates the transduction channel complex in Caenorhabditis elegans touch receptor neurons. J. Neurosci. *31*, 12695–12704.

Aumailley, M. (2013). The laminin family. Cell Adhes. Migr. *7*, 48–55.

Aumailley, M. (2021). Laminins and interaction partners in the architecture of the basement membrane at the dermal-epidermal junction. Exp. Dermatol. *30*, 17–24.

Aumailley, M., Battaglia, C., Mayer, U., Reinhardt, D., Nischt, R., Timpl, R., and Fox, J.W. (1993). Nidogen mediates the formation of ternary complexes of basement membrane components. Kidney Int. *43*, 7–12.

Baconguis, I., Bohlen, C.J., Goehring, A., Julius, D., and Gouaux, E. (2014). X-ray structure of acid-sensing ion channel 1-snake toxin complex reveals open state of a Na+-selective channel. Cell *156*, 717–729.

Bader, B.L., Smyth, N., Nedbal, S., Miosge, N., Baranowsky, A., Mokkapati, S., Murshed, M., and Nischt, R. (2005). Compound genetic ablation of nidogen 1 and 2 causes basement membrane defects and perinatal lethality in mice. Mol. Cell. Biol. *25*, 6846–6856.

Böse, K., Nischt, R., Page, A., Bader, B.L., Paulsson, M., and Smyth, N. (2006). Loss of nidogen-1 and -2 results in syndactyly and changes in limb development. J. Biol. Chem. *281*, 39620–39629.

Bianchi, L., and Driscoll, M. (2006). Culture of embryonic C. elegans cells for electrophysiological and pharmacological analyses. WormBook 1–15.

Cascio, C.J., Moore, D., and McGlone, F. (2019). Social touch and human development. Dev. Cogn. Neurosci. *35*, 5–11.

Chalfie, M., and Au, M. (1989). Genetic control of differentiation of the Caenorhabditis elegans touch receptor neurons. Science 243, 1027–1033.

Chalfie, M., and Sulston, J. (1981). Developmental genetics of the mechanosensory neurons of

Caenorhabditis elegans. Dev. Biol. 82, 358–370.
Chelur, D.S., Ernstrom, G.G., Goodman, M.B., Yao, C.A., Chen, L., O'Hagan, R., Chalfie, M., O' Hagan, R., Chalfie, M., O'Hagan, R., et al. (2002). The mechanosensory protein MEC-6 is a subunit of the C. elegans touch-cell degenerin channel. Nature *420*, 669–673.
Chen, X., and Chalfie, M. (2014). Modulation of C. elegans touch sensitivity is integrated at multiple levels. J. Neurosci. *34*, 6522–6536.
Chen, X., and Chalfie, M. (2015). Regulation of mechanosensation in C. elegans through ubiquitination of the MEC-4 mechanotransduction channel. J. Neurosci. *35*, 2200–2212.
Chiang, L.Y., Poole, K., Oliveira, B.E., Duarte, N., Sierra, Y.A.B., Bruckner-Tuderman, L., Koch, M., Hu, J., and Lewin, G.R. (2011). Laminin-332 coordinates mechanotransduction and growth cone bifurcation in sensory neurons. Nat. Neurosci. *14*, 993–1000.
Christensen, M., and Strange, K. (2001). Developmental Regulation of a Novel Outwardly Rectifying Mechanosensitive Anion Channel in Caenorhabditis elegans *. J. Biol. Chem. *276*, 45024–45030.
Christensen, M., Estevez, A., Yin, X., Fox, R., Morrison, R., McDonnell, M., Gleason, C., Miller, D.M., and Strange, K. (2002). A primary culture system for functional analysis of C. elegans neurons and muscle cells. Neuron *33*, 503–514.
Clay, M.R., and Sherwood, D.R. (2015). Basement Membranes in the Worm: A Dynamic Scaffolding that Instructs Cellular Behaviors and Shapes Tissues. Curr. Top. Membr. *76*, 337–371.
Coakley, S., Ritchie, F.K., Galbraith, K.M., and Hilliard, M.A. (2020). Epidermal control of axonal attachment via β-spectrin and the GTPase-activating protein TBC-10 prevents axonal degeneration. Nat. Commun. *11*, 1–12.
Cristofori-Armstrong, B., and Rash, L.D. (2017). Acid-sensing ion channel (ASIC) structure and function: Insights from spider, snake and sea anemone venoms. Neuropharmacology *127*, 173–184.
Cueva, J.G., Mulholland, A., and Goodman, M.B. (2007). Nanoscale organization of the MEC-4 DEG/ENaC sensory mechanotransduction channel in Caenorhabditis elegans touch receptor neurons. J. Neurosci. *27*, 14089–14098.
Dai, J., Estrada, B., Jacobs, S., Sánchez-Sánchez, B.J., Tang, J., Ma, M., Magadán-Corpas, P., Pastor-Pareja, J.C., and Martín-Bermudo, M.D. (2018). Dissection of Nidogen function in Drosophila reveals tissue-specific mechanisms of basement membrane assembly. PLoS Genet. *14*, e1007483.

Díaz-Balzac, C.A., Rahman, M., Lázaro-Peña, M.I., Martin Hernandez, L.A., Salzberg, Y., Aguirre-Chen, C., Kaprielian, Z., and Bülow, H.E. (2016). Muscle- and Skin-Derived Cues Jointly Orchestrate Patterning of Somatosensory Dendrites. Curr. Biol. *26*, 2379–2387.
Dickinson, D.J., Pani, A.M., Heppert, J.K., Higgins, C.D., and Goldstein, B. (2015). Streamlined genome engineering with a self-excising drug selection cassette. Genetics *200*, 1035–1049.
Domogatskaya, A., Rodin, S., and Tryggvason, K. (2012). Functional Diversity of Laminins. Annu. Rev. Cell Dev. Biol. *28*, 523–553.
Dong, L., Chen, Y., Lewis, M., Hsieh, J.C., Reing, J., Chaillet, J.R., Howell, C.Y., Melhem, M., Inoue, S., Kuszak, J.R., et al. (2002). Neurologic defects and selective disruption of basement membranes in mice lacking entactin-1/nidogen-1. Lab. Invest. *82*, 1617–1630.
Driscoll, M., and Chalfie, M. (1991). The mec-4 gene is a member of a family of Caenorhabditis elegans genes that can mutate to induce neuronal degeneration. Nature *349*, 588–593.
Du, H., Gu, G., William, C.M., and Chalfie, M. (1996). Extracellular proteins needed for C. elegans mechanosensation. Neuron *16*, 183–194.
Eastwood, A.L., Sanzeni, A., Petzold, B.C., Park, S.J., Vergassola, M., Pruitt, B.L., and Goodman, M.B. (2015). Tissue mechanics govern the rapidly adapting and symmetrical response to touch. Proc. Natl. Acad. Sci. U. S. A. *112*, E6955–E6963.
Emtage, L., Gu, G., Hartwieg, E., and Chalfie, M. (2004). Extracellular proteins organize the mechanosensory channel complex in C. elegans touch receptor neurons. Neuron *44*, 795–807.
Ernstrom, G.G., and Chalfie, M. (2003). Genetics of Sensory Mechanotransduction. Annu. Rev. Genet. 36, 411–453.
Forrester, W.C., Perens, E., Zallen, J.A., and Garriga, G. (1998). Identification of Caenorhabditis elegans Genes Required for Neuronal Differentiation and Migration. Genetics *148*, 151–165.
Fox, J.W., Mayer, U., Nischt, R., Aumailley, M., Reinhardt, D., Wiedemann, H., Mann, K., Timpl, R., Krieg, T., and Engel, J. (1991). Recombinant nidogen consists of three globular domains and mediates binding of laminin to collagen type IV. EMBO J. *10*, 3137–3146.
Franco, J.A. (2021). Methods for robust measurements in low signal-to-noise systems and their application to nematode mechanoreceptors.
Han, C., Wang, D., Soba, P., Zhu, S., Lin, X., Jan, L.Y., and Jan, Y.N. (2012). Integrins Regulate Repulsion-Mediated Dendritic Patterning of Drosophila Sensory Neurons by Restricting Dendrites in a 2D Space. Neuron *73*, 64–78.
Heppert, J.K., Dickinson, D.J., Pani, A.M., Higgins, C.D., Steward, A., Ahringer, J., Kuhn, J.R., and Goldstein, B. (2016). Comparative assessment of fluorescent proteins for in vivo imaging in

an animal model system. Mol. Biol. Cell *27*, 3385–3394.
Hill, P.S.M. (2008). Vibrational Communication in Animals (Cambridge, Mass. : Harvard University Press).
Hostettler, L., Grundy, L., Käser-Pébernard, S., Wicky, C., Schafer, W.R., and Glauser, D.A. (2017). The bright fluorescent protein mNeonGreen facilitates protein expression analysis in vivo. G3 *7*, 607–615.
Huang, C.C., Hall, D.H., Hedgecock, E.M., Kao, G., Karantza, V., Vogel, B.E., Hutter, H., Chisholm, A.D., Yurchenco, P.D., and Wadsworth, W.G. (2003). Laminin α subunits and their role in C. elegans development. Development *130*, 3343–3358.
Hynes, R.O. (2012). The evolution of metazoan extracellular matrix. J. Cell Biol. *196*, 671–679.
Jiang, N., Rasmussen, J.P., Clanton, J.A., Rosenberg, M.F., Luedke, K.P., Cronan, M.R., Parker, E.D., Kim, H.-J., Vaughan, J.C., Sagasti, A., et al. (2019). A conserved morphogenetic mechanism for epidermal ensheathment of nociceptive sensory neurites. Elife *8*, e42455.
Kang, S.H., and Kramer, J.M. (2000). Nidogen is nonessential and not required for normal type IV collagen localization in Caenorhabditis elegans. Mol. Biol. Cell *11*, 3911–3923.
Kao, G., Huang, C.-C.C., Hedgecock, E.M., Hall, D.H., and Wadsworth, W.G. (2006). The role of the laminin beta subunit in laminin heterotrimer assembly and basement membrane function and development in C. elegans. Dev. Biol. *290*, 211–219.
Katta, S., Krieg, M., and Goodman, M.B. (2015). Feeling Force: Physical and Physiological Principles Enabling Sensory Mechanotransduction. Annu. Rev. Cell Dev. Biol. *31*, 347–371.
Katta, S., Sanzeni, A., Das, A., Vergassola, M., and Goodman, M.B. (2019). Progressive recruitment of distal MEC-4 channels determines touch response strength in C. elegans. J. Gen. Physiol. *151*, 1213–1230.
Keeley, D.P., Hastie, E., Jayadev, R., Kelley, L.C., Chi, Q., Payne, S.G., Jeger, J.L., Hoffman, B.D., and Sherwood, D.R. (2020). Comprehensive Endogenous Tagging of Basement Membrane Components Reveals Dynamic Movement within the Matrix Scaffolding. Dev. Cell *54*, 60-74.e7.
Kim, S., and Wadsworth, W.G. (2000). Positioning of Longitudinal Nerves in C. elegans by Nidogen. Science (80-.). *288*, 150–154.
Kramer, J.M. (2003). Genetic analysis of extracellular matrix in C. elegans. Annu. Rev. Genet. *28*, 95–116.
Krieg, M., Stühmer, J., Cueva, J.G., Fetter, R., Spilker, K., Cremers, D., Shen, K., Dunn, A.R., and Goodman, M.B. (2017). Genetic defects in β-spectrin and tau sensitize C. Elegans axons to

movement-induced damage via torque-tension coupling. Elife *6*.
Kung, C. (2005). A possible unifying principle for mechanosensation. Nat. Cell Biol. *436*, 647–654.
Li, Q., Lau, A., Morris, T.J., Guo, L., Fordyce, C.B., and Stanley, E.F. (2004). A syntaxin 1, Galpha(o), and N-type calcium channel complex at a presynaptic nerve terminal: analysis by quantitative immunocolocalization. J. Neurosci. *24*, 4070–4081.
Lockhead, D., Schwarz, E.M., O'hagan, R., Bellotti, S., Krieg, M., Barr, M.M., Dunn, A.R., Sternberg, P.W., and Goodman, M.B. (2016). The tubulin repertoire of Caenorhabditis elegans sensory neurons and its context-dependent role in process outgrowth. Mol. Biol. Cell *27*, 3717–3728.
Mann, K., Deutzmann, R., and Timpl, R. (1988). Characterization of proteolytic fragments of the laminin-nidogen complex and their activity in ligand-binding assays. Eur. J. Biochem. *178*, 71–80.
Mann, K., Deutzmann, R., Aumailley, M., Timpl, R., Raimondi, L., Yamada, Y., Pan, T.C., Conway, D., and Chu, M.L. (1989). Amino acid sequence of mouse nidogen, a multidomain basement membrane protein with binding activity for laminin, collagen IV and cells. EMBO J. *8*, 65.
Mayer, U., Kohfeldt, E., and Timpl, R. (1998). Structural and genetic analysis of laminin-nidogen interaction. In Annals of the New York Academy of Sciences, (New York Academy of Sciences), pp. 130–142.
Mezulis, S., Yates, C.M., Wass, M.N., E Sternberg, M.J., and Kelley, L.A. (2015). The Phyre2 web portal for protein modeling, prediction and analysis. Nat. Protoc. *10*, 845–858.
Mishra, M. (2020). Evolutionary Aspects of the Structural Convergence and Functional Diversification of Kunitz-Domain Inhibitors. J. Mol. Evol. *88*, 537–548.
El Mouridi, S., Lecroisey, C., Tardy, P., Mercier, M., Leclercq-Blondel, A., Zariohi, N., and Boulin, T. (2017). Reliable CRISPR/Cas9 genome engineering in Caenorhabditis elegans using a single efficient sgRNA and an easily recognizable phenotype. G3 Genes, Genomes, Genet. *7*, 1429–1437.
Muriel, J.M., Dong, C., Hutter, H., and Vogel, B.E. (2005). Fibulin-1C and Fibulin-1D splice variants have distinct functions and assemble in a hemicentin-dependent manner. Development *132*, 4223–4234.
Murshed, M., Smyth, N., Miosge, N., Karolat, J., Krieg, T., Paulsson, M., and Nischt, R. (2000). The absence of nidogen 1 does not affect murine basement membrane formation. Mol. Cell.

Biol. *20*, 7007–7012.
Nekimken, A.L., Mazzochette, E.A., Goodman, M.B., and Pruitt, B.L. (2017). Forces applied during classical touch assays for Caenorhabditis elegans. PLoS One *12*.
Nekimken, A.L., Pruitt, B.L., and Goodman, M.B. (2020). Touch-induced mechanical strain in somatosensory neurons is independent of extracellular matrix mutations in Caenorhabditis elegans. Mol. Biol. Cell *31*, 1735–1743.
O'Brien, G.S., Rieger, S., Wang, F., Smolen, G.A., Gonzalez, R.E., Buchanan, J., and Sagasti, A. (2012). Coordinate development of skin cells and cutaneous sensory axons in zebrafish. J. Comp. Neurol. *520*, 816–831.
O'Hagan, R., Chalfie, M., and Goodman, M.B. (2005). The MEC-4 DEG/ENaC channel of Caenorhabditis elegans touch receptor neurons transduces mechanical signals. Nat. Neurosci. *8*, 43–50.
Paix, A., Folkmann, A., Rasoloson, D., and Seydoux, G. (2015). High Efficiency, Homology-Directed Genome Editing in Caenorhabditis elegans Using CRISPR-Cas9 Ribonucleoprotein Complexes. Genetics *201*, 47–54.
Patel, T.R., Bernards, C., Meier, M., McEleney, K., Winzor, D.J., Koch, M., and Stetefeld, J. (2014). Structural elucidation of full-length nidogen and the laminin-nidogen complex in solution. Matrix Biol. *33*, 60–67.
Peng, A.W., and Ricci, A.J. (2016). Glass Probe Stimulation of Hair Cell Stereocilia. Methods Mol. Biol. 1427, 487–500.
Petzold, B.C., Park, S.J., Mazzochette, E.A., Goodman, M.B., and Pruitt, B.L. (2013). MEMS-based force-clamp analysis of the role of body stiffness in C. elegans touch sensation. Integr. Biol. (United Kingdom) *5*, 853–864.
Poschl, E., Fox, J.W., Block, D., Mayer, U., and Timpl, R. (1994). Two non-contiguous regions contribute to nidogen binding to a single EGF-like motif of the laminin gamma 1 chain. EMBO J. *13*, 3741.
Pöschl, E., Mayer, U., Stetefeld, J., Baumgartner, R., Holak, T.A., Huber, R., and Timpl, R. (1996). Site-directed mutagenesis and structural interpretation of the nidogen binding site of the laminin γ1 chain. EMBO J. *15*, 5154–5159.
Powers, R.J., Roy, S., Atilgan, E., Brownell, W.E., Sun, S.X., Gillespie, P.G., and Spector, A.A. (2012). Stereocilia Membrane Deformation: Implications for the Gating Spring and Mechanotransduction Channel. Biophys. J. *102*, 201.
Rhiner, C., Gysi, S., Fröhli, E., Hengartner, M.O., and Hajnal, A. (2005). Syndecan regulates cell

migration and axon guidance in C. elegans. Development *132*, 4621–4633.
Rivera Gomez, K., and Schvarzstein, M. (2018). Immobilization of nematodes for live imaging using an agarose pad produced with a Vinyl Record. MicroPublication Biol. *2018*.
Rogers, R.S., and Nishimune, H. (2017). The role of laminins in the organization and function of neuromuscular junctions. Matrix Biol. *57–58*, 86–105.
Sanes, J.R., and Lichtman, J.W. (1999). Development of the vertebrate neuromuscular junction. Annu. Rev. Neurosci. *22*, 389–442.
Sangaletti, R., and Bianchi, L. (2013). A method for culturing embryonic C. elegans cells. J. Vis. Exp.
Sangaletti, R., Dahl, G., and Bianchi, L. (2014). Mechanosensitive unpaired innexin channels in C. elegans touch neurons. Am. J. Physiol. - Cell Physiol. *307*, C966–C977.
Sanzeni, A., Katta, S., Petzold, B., Pruitt, B.L., Goodman, M.B., and Vergassola, M. (2019). Somatosensory neurons integrate the geometry of skin deformation and mechanotransduction channels to shape touch sensing. Elife *8*.
Schymeinsky, J., Nedbal, S., Miosge, N., Pöschl, E., Rao, C., Beier, D.R., Skarnes, W.C., Timpl, R., and Bader, B.L. (2002). Gene structure and functional analysis of the mouse nidogen-2 gene: nidogen-2 is not essential for basement membrane formation in mice. Mol. Cell. Biol. *22*, 6820–6830.
Stiernagle, T. (2006). Maintenance of C. elegans. WormBook 1–11.
Strale, P.O., Azioune, A., Bugnicourt, G., Lecomte, Y., Chahid, M., and Studer, V. (2016). Multiprotein Printing by Light-Induced Molecular Adsorption. Adv. Mater. *28*, 2024–2029.
Strange, K., Christensen, M., and Morrison, R. (2007). Primary culture of Caenorhabditis elegans developing embryo cells for electrophysiological, cell biological and molecular studies. Nat. Protoc. *2*, 1003–1012.
Suzuki, H., Kerr, R., Bianchi, L., Frøkjaer-Jensen, C., Slone, D., Xue, J., Gerstbrein, B., Driscoll, M., and Schafer, W.R. (2003). In vivo imaging of *C. elegans* mechanosensory neurons demonstrates a specific role for the MEC-4 channel in the process of gentle touch sensation. Neuron *39*, 1005–1017.
Takagi, J., Yang, Y., Liu, J., Wang, J., and Springer, T.A. (2003). Complex between nidogen and laminin fragments reveals a paradigmatic β-propeller interface. Nature *424*, 969–974.
Talagas, M., Lebonvallet, N., Leschiera, R., Elies, P., Marcorelles, P., and Misery, L. (2020). Intra-epidermal nerve endings progress within keratinocyte cytoplasmic tunnels in normal human skin. Exp. Dermatol. *29*, 387–392.

Taylor, S.R., Santpere, G., Weinreb, A., Barrett, A., Reilly, M.B., Xu, C., Varol, E., Oikonomou, P., Glenwinkel, L., McWhirter, R., et al. (2021). Molecular topography of an entire nervous system. Cell *184*, 4329-4347.e23.

Vásquez, V., Krieg, M., Lockhead, D., and Goodman, M.B. (2014). Phospholipids that contain polyunsaturated fatty acids enhance neuronal cell mechanics and touch sensation. Cell Rep. *6*, 70–80.

Vogel, B.E., and Hedgecock, E.M. (2001). Hemicentin, a conserved extracellular member of the immunoglobulin superfamily, organizes epithelial and other cell attachments into oriented line-shaped junctions. Development *128*, 883–894.

Wolfstetter, G., Dahlitz, I., Pfeifer, K., Töpfer, U., Alt, J.A., Pfeifer, D.C., Lakes-Harlan, R., Baumgartner, S., Palmer, R.H., and Holz, A. (2019). Characterization of Drosophila Nidogen/entactin reveals roles in basement membrane stability, barrier function and nervous system patterning. Dev. *146*.

Yin, C., Peterman, E., Rasmussen, J.P., and Parrish, J.Z. (2021). Transparent Touch: Insights From Model Systems on Epidermal Control of Somatosensory Innervation. Front. Cell. Neurosci. *15*, 1–21.

Yurchenco, P.D., Quan, Y., Colognato, H., Mathus, T., Harrison, D., Yamada, Y., and O'rear, J.J. (1997). The chain of laminin-1 is independently secreted and drives secretion of its β- and γ-chain partners.

Zhang, Y., Ma, C., Delohery, T., Nasipak, B., Foat, B.C., Bounoutas, A., Bussemaker, H.J., Kim, S.K., and Chalfie, M. (2002). Identification of genes expressed in C. elegans touch receptor neurons. Nature *418*, 331–335.

Zheng, C., Diaz-Cuadros, M., and Chalfie, M. (2015). Hox Genes Promote Neuronal Subtype Diversification through Posterior Induction in Caenorhabditis elegans. Neuron *88*, 514–527.

FIGURE 1

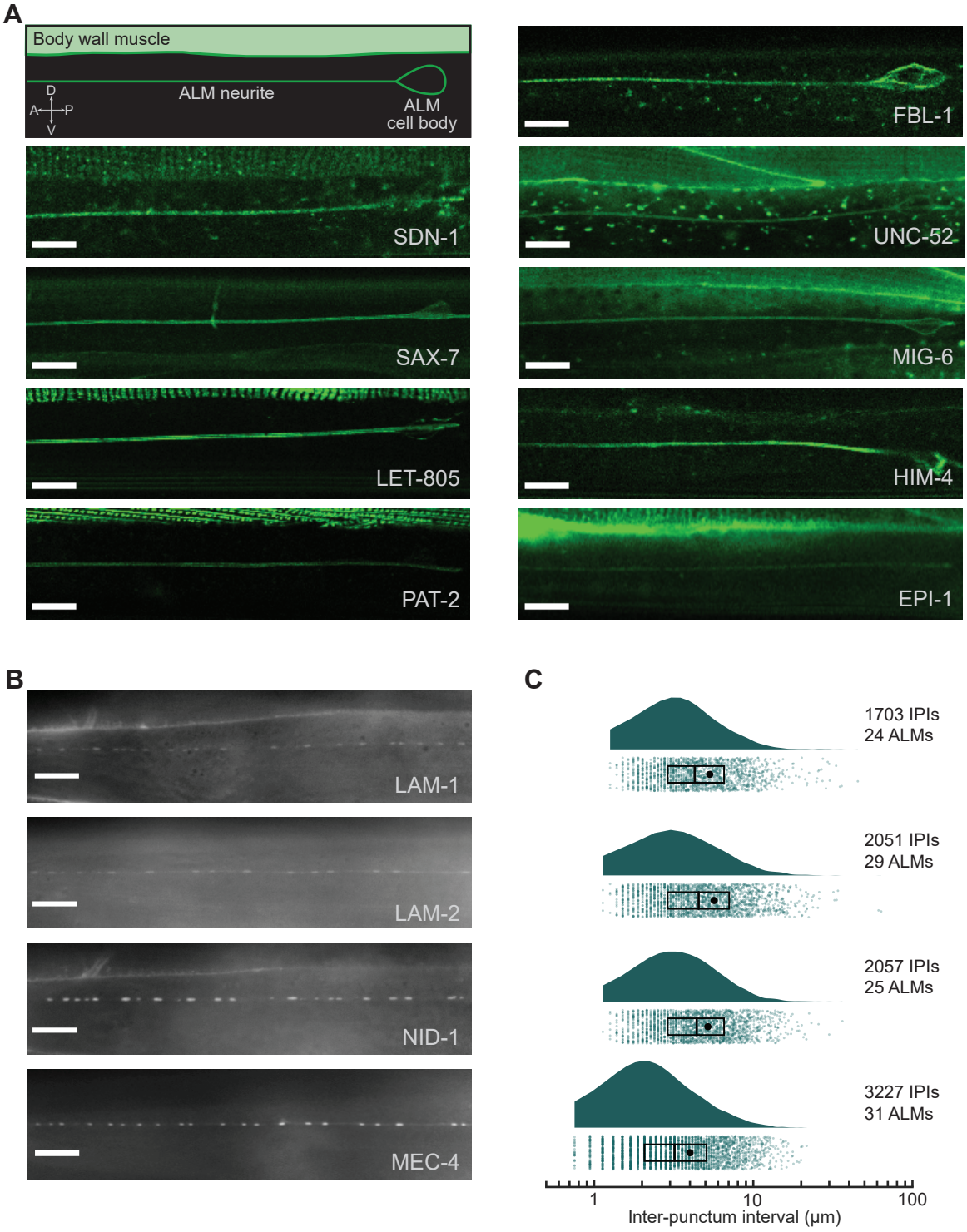
A
Body wall muscle
ALM neurite
ALM
cell body
D
A
P
V
FBL-1
SDN-1
UNC-52
SAX-7
MIG-6
LET-805
HIM-4
PAT-2
EPI-1
B
LAM-1
LAM-2
NID-1
MEC-4
C
1703 IPIs
24 ALMs
2051 IPIs
29 ALMs
2057 IPIs
25 ALMs
3227 IPIs
31 ALMs
1
10
100
Inter-punctum interval (μm)

FIGURE 2

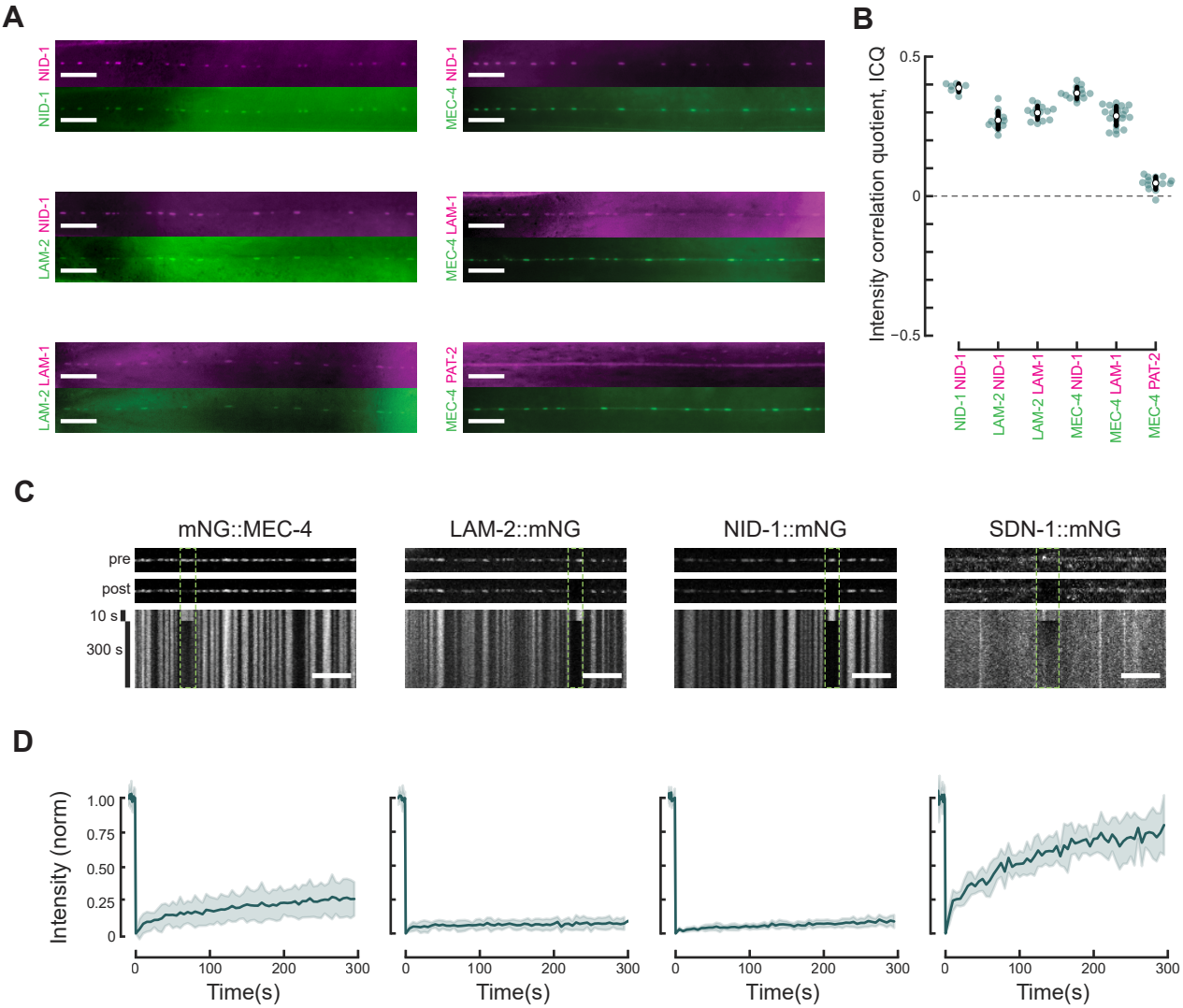
A
NID-1 NID-1
NID-1 MEC-4
LAM-2 NID-1
MEC-4 LAM-1
LAM-2 LAM-1
MEC-4 PAT-2
B
Intensity correlation quotient, ICQ
0.5
0
−0.5
NID-1 NID-1
LAM-2 NID-1
LAM-2 LAM-1
MEC-4 NID-1
MEC-4 LAM-1
MEC-4 PAT-2
C
mNG::MEC-4
LAM-2::mNG
NID-1::mNG
SDN-1::mNG
pre
post
10 s
300 s
D
Intensity (norm)
1.00
0.75
0.50
0.25
0
0
100
200
300
Time(s)

FIGURE 3

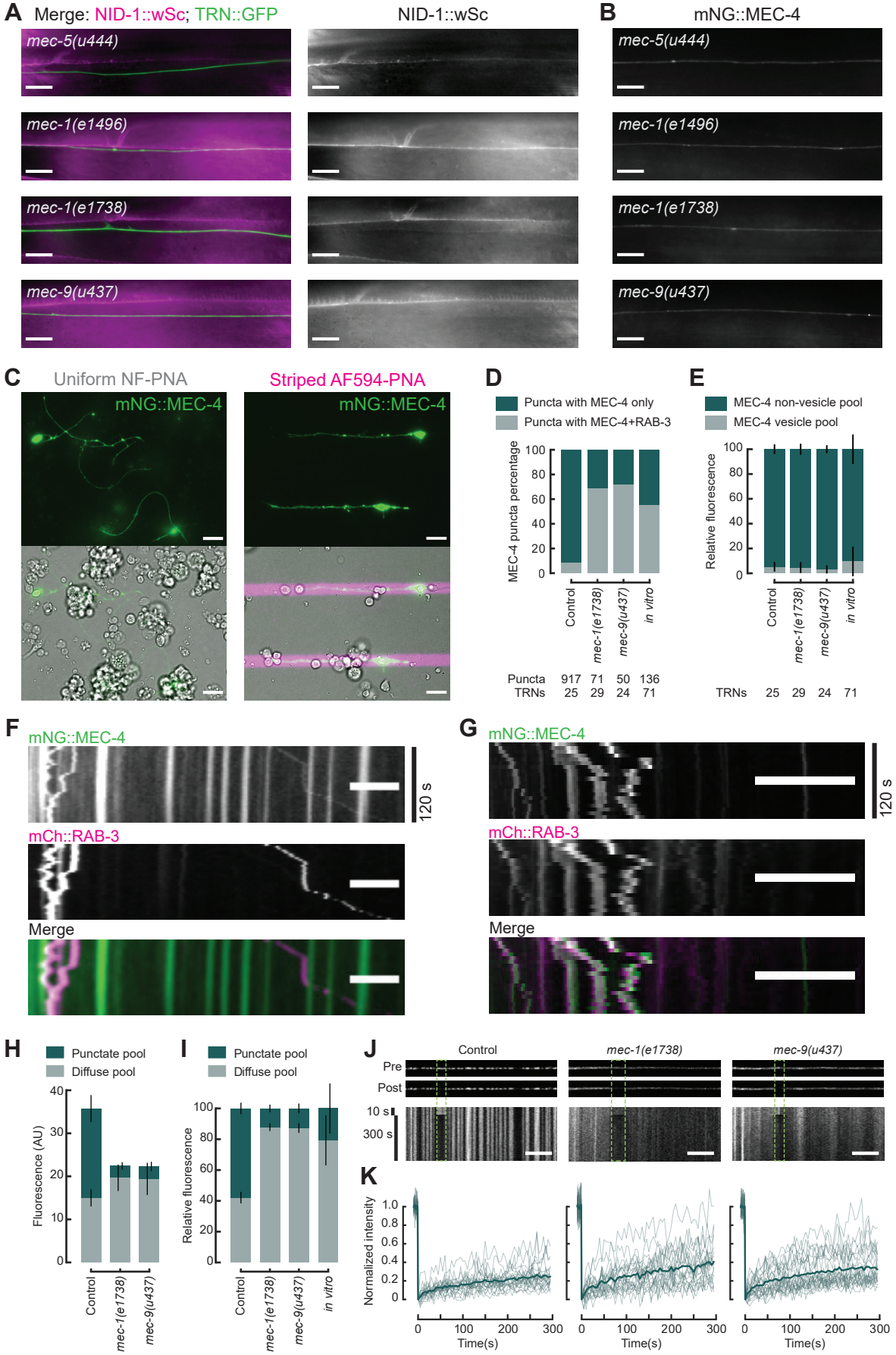
A
Merge: NID-1::wSc; TRN::GFP
NID-1::wSc
B
mNG::MEC-4
mec-5(u444)
mec-1(e1496)
mec-1(e1738)
mec-9(u437)
C
Uniform NF-PNA
Striped AF594-PNA
mNG::MEC-4
D
Puncta with MEC-4 only
Puncta with MEC-4+RAB-3
MEC-4 puncta percentage
Control
mec-1(e1738)
mec-9(u437)
in vitro
Puncta 917 71 50 136
TRNs 25 29 24 71
E
MEC-4 non-vesicle pool
MEC-4 vesicle pool
Relative fluorescence
TRNs 25 29 24 71
F
mNG::MEC-4
mCh::RAB-3
Merge
120 s
G
mNG::MEC-4
mCh::RAB-3
Merge
120 s
H
Punctate pool
Diffuse pool
Fluorescence (AU)
I
Punctate pool
Diffuse pool
Relative fluorescence
J
Control
mec-1(e1738)
mec-9(u437)
Pre
Post
10 s
300 s
K
Normalized intensity
Time(s)

FIGURE 4

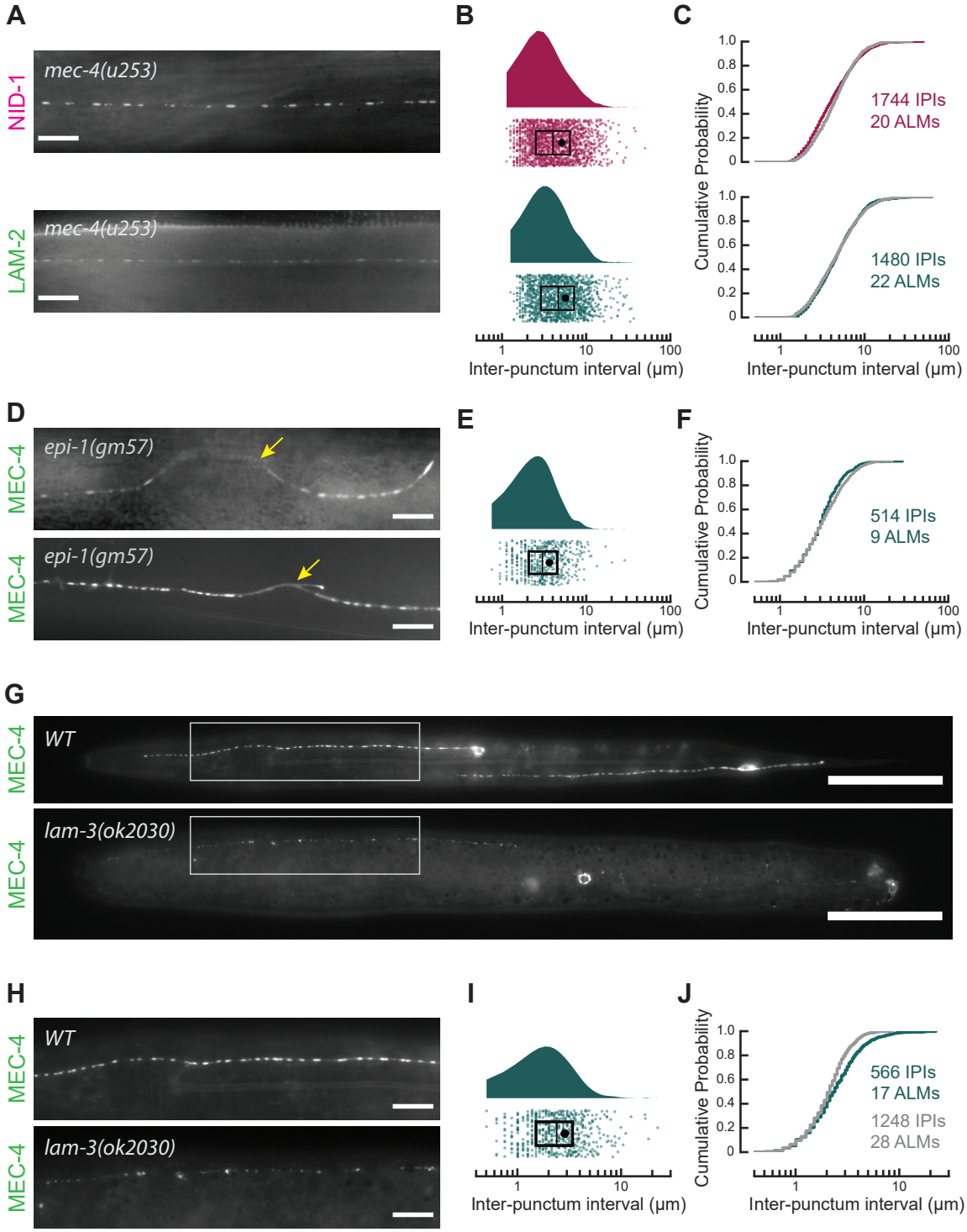
A
NID-1
mec-4(u253)
LAM-2
mec-4(u253)
B
C
Cumulative Probability
1744 IPIs
20 ALMs
1480 IPIs
22 ALMs
Inter-punctum interval (μm)
D
MEC-4
epi-1(gm57)
MEC-4
epi-1(gm57)
E
F
514 IPIs
9 ALMs
G
MEC-4
WT
MEC-4
lam-3(ok2030)
H
MEC-4
WT
MEC-4
lam-3(ok2030)
I
J
566 IPIs
17 ALMs
1248 IPIs
28 ALMs

FIGURE 5

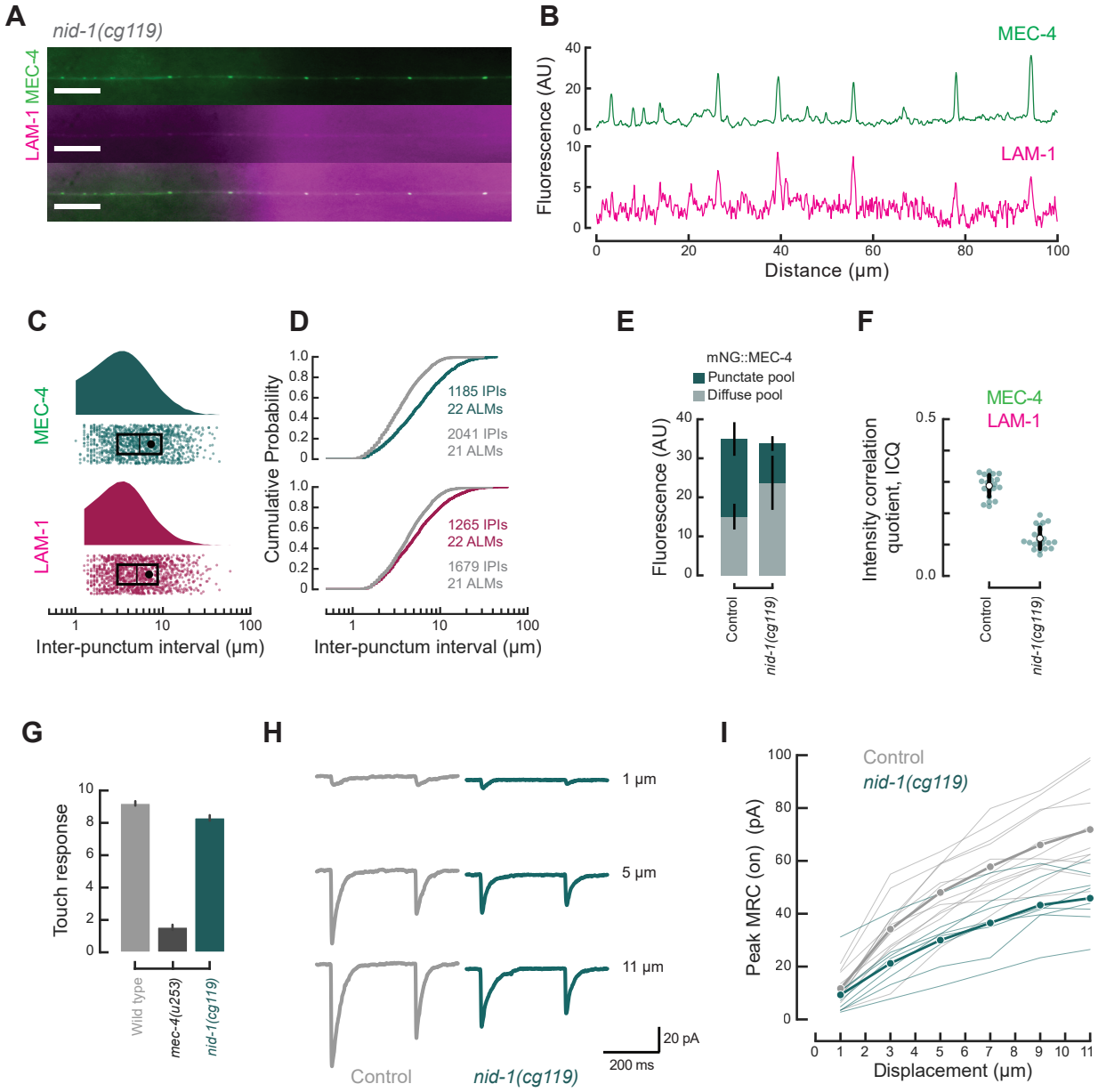
A
nid-1(cg119)
LAM-1 MEC-4
B
MEC-4
LAM-1
Fluorescence (AU)
Distance (µm)
C
MEC-4
LAM-1
Inter-punctum interval (µm)
D
Cumulative Probability
1185 IPIs
22 ALMs
2041 IPIs
21 ALMs
1265 IPIs
22 ALMs
1679 IPIs
21 ALMs
Inter-punctum interval (µm)
E
mNG::MEC-4
Punctate pool
Diffuse pool
Fluorescence (AU)
Control
nid-1(cg119)
F
MEC-4
LAM-1
Intensity correlation quotient, ICQ
Control
nid-1(cg119)
G
Touch response
Wild type
mec-4(u253)
nid-1(cg119)
H
1 µm
5 µm
11 µm
20 pA
200 ms
Control
nid-1(cg119)
I
Control
nid-1(cg119)
Peak MRC (on) (pA)
Displacement (µm)

FIGURE 6

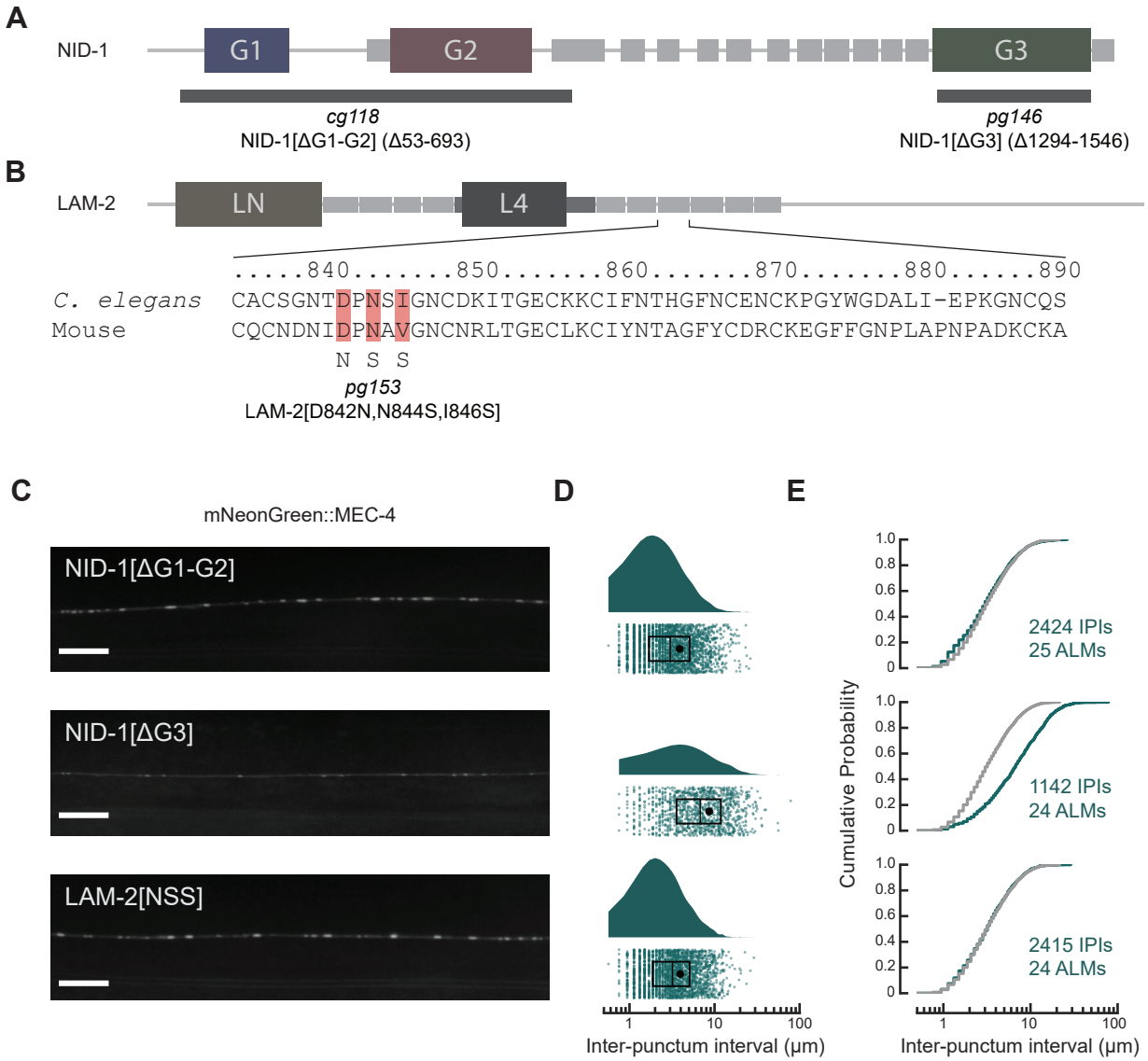
A
NID-1
G1
G2
G3
cg118
NID-1[ΔG1-G2] (Δ53-693)
pg146
NID-1[ΔG3] (Δ1294-1546)
B
LAM-2
LN
L4
.....840.....850.....860.....870.....880.....890
C. elegans CACSGNTDPNSIGNCDKITGECKKCIFNTHGFNCENCKPGYWGDALI-EPKGNCQS
Mouse CQCNDNIDPNAVGNCNRLTGECLKCIYNTAGFYCDRCKEGFFGNPLAPNPADKCKA
N S S
pg153
LAM-2[D842N,N844S,I846S]
C
mNeonGreen::MEC-4
NID-1[ΔG1-G2]
NID-1[ΔG3]
LAM-2[NSS]
D
1
10
100
Inter-punctum interval (μm)
E
Cumulative Probability
1.0
0.8
0.6
0.4
0.2
0
2424 IPIs
25 ALMs
1142 IPIs
24 ALMs
2415 IPIs
24 ALMs
1
10
100
Inter-punctum interval (μm)

FIGURE 7

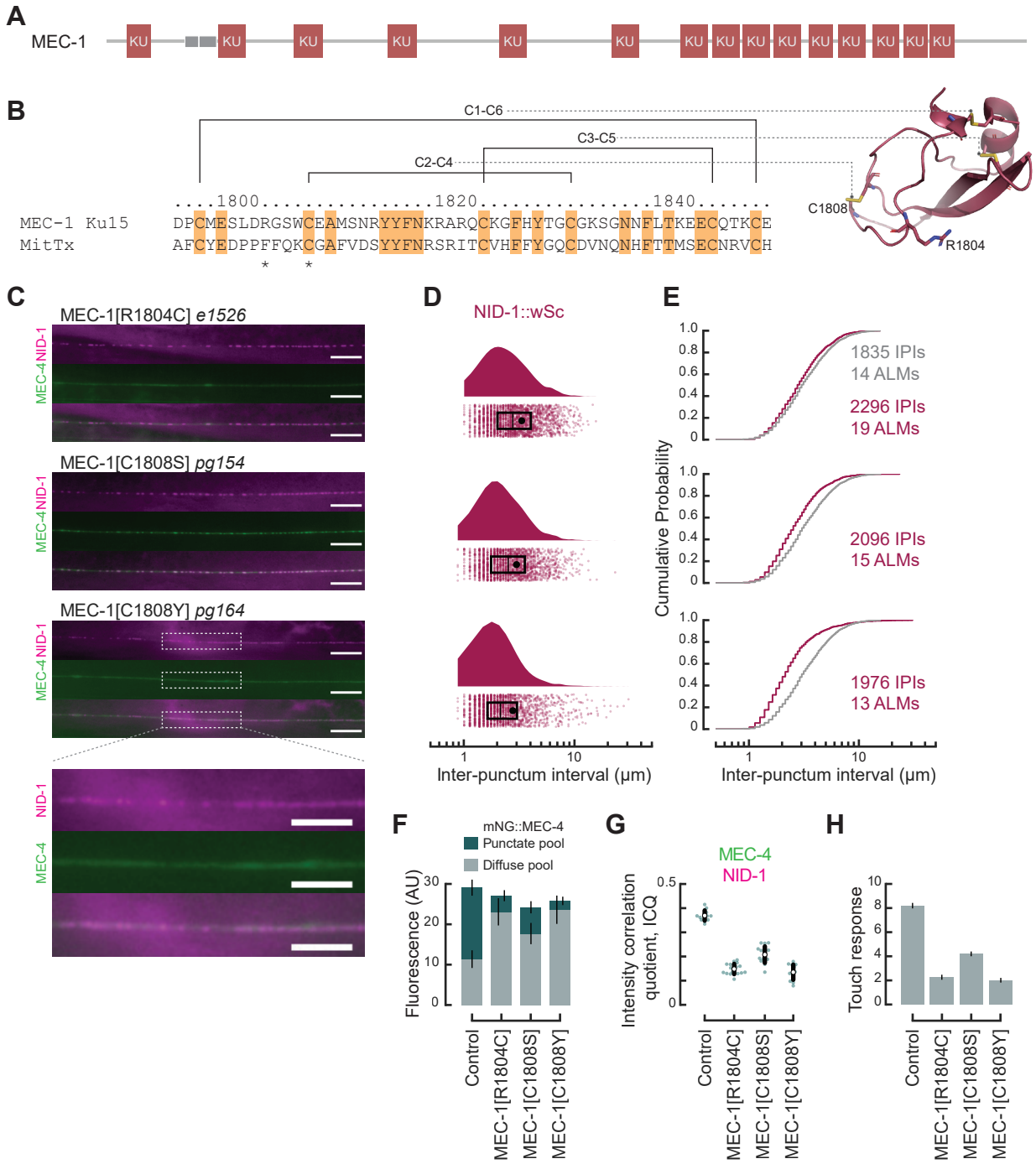
A
MEC-1
KU
B
C1-C6
C3-C5
C2-C4
....1800.....1820.....1840.....
MEC-1 Ku15 DPCMESLDRGSWCEAMSNRYYFNKRARQCKGFHYTGCGKSGNNFLTKEECQTKCE
MitTx AFCYEDPPFFQKCGAFVDSYYFNRSRITCVHFFYGQCDVNQNHFTTMSECNRVCH
C1808
R1804
C
MEC-1[R1804C] e1526
MEC-1[C1808S] pg154
MEC-1[C1808Y] pg164
NID-1
MEC-4
D
NID-1::wSc
Inter-punctum interval (μm)
E
Cumulative Probability
1835 IPIs
14 ALMs
2296 IPIs
19 ALMs
2096 IPIs
15 ALMs
1976 IPIs
13 ALMs
Inter-punctum interval (μm)
F
mNG::MEC-4
Punctate pool
Diffuse pool
Fluorescence (AU)
Control
MEC-1[R1804C]
MEC-1[C1808S]
MEC-1[C1808Y]
G
MEC-4
NID-1
Intensity correlation quotient, ICQ
H
Touch response

FIGURE 8

A

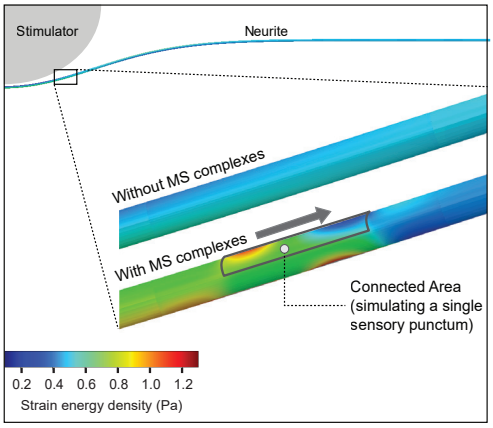
Stimulator
Neurite
Without MS complexes
With MS complexes
Connected Area
(simulating a single
sensory punctum)
0.2 0.4 0.6 0.8 1.0 1.2
Strain energy density (Pa)

B

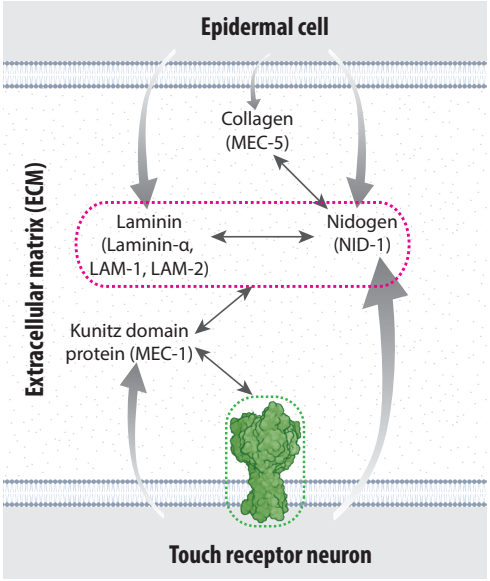
Epidermal cell
Collagen
(MEC-5)
Extracellular matrix (ECM)
Laminin
(Laminin-α,
LAM-1, LAM-2)
Nidogen
(NID-1)
Kunitz domain
protein (MEC-1)
Touch receptor neuron

Table S1. List of all strains used in screening for localization of proteins along TRNs

Strain name	Genotype	Fluorescence visible around TRNs: Widefield	Fluorescence visible around TRNs: Confocal	Uniform or punctate?
NK2353	*agr-1 (qy27[agr-1::mNG+loxP]) II*	No	No	
NK2456	*ddr-1(qy43[ddr-1::mNG+loxP]) X*	No	No	
NK2457	*ddr-2(qy44[ddr-2::mNG+loxP]) X*	No	No	
NK2318	*dgn-1(qy18[dgn-1::mNG]) X*	No	No	
NK2604	*emb-9 (qy89[emb-9::mEos2+loxP]) II*	No	No	
NK2404	*epi-1(qy31[epi-1::mNG+loxP]) IV.*	No	Yes	Uniform
NK2579	*fbl-1(qy62[mNG+loxP::fbl-1]) IV*	Yes	Yes	Uniform
NK2590	*gon-1(qy45[gon-1::mNG+loxP]) IV*	No	Not tested	
NK2581	*gpn-1(qy35[gpn-1::mNG+loxP]) X*	No	Not tested	
NK2422	*him-4(qy33[him-4::mNG+loxP]) IV.*	Yes	Yes	Uniform
LP172	*hmr-1(cp21[hmr-1::GFP + LoxP]) I*	No	Not tested	
NK2476	*ina-1(qy46[ina-1::mKate+loxP]) III*	No	Not tested	
GN896	*lam-1(pg136[lam-1::wSc]) IV*	Yes	Not tested	Punctate
NK2335	*lam-2(qy20[lam-2::mNG+LoxP]) X*	Yes	Yes	Punctate
NK2425	*lam-3(qy28[lam-3::mNG+loxP]) I.*	No	No	
NK2558	*let-2(qy61[let-2::mNG+loxP]) X*	No	Not tested	
ML2501	*let-805(mc73[let-805::gfp + unc-119(+)]) unc-119(ed3) III*	Yes	Yes	Uniform
NK2582	*lon-2(qy55[lon-2::mNG+loxP]) X*	No	Not tested	
FDU1056	*mig-17(shc19[mig-17::mNG +LoxP])*	No	Not tested	
NK2442	*mig-6(qy37[mNG+loxP::mig-6]) V*	Yes	Yes	Uniform
NK2557	*mig-6(qy73[mig-6::mNG+loxP]) V*	No	Not tested	
NK2443	*nid-1(qy38[nid-1::mNG+loxP]) V.*	Yes	Yes	Punctate
NK2479	*pat-2(qy49[pat-2::2xmNG]) III*	Yes	Yes	Uniform
NK2477	*ptp-3(qy47[ptp-3::mNG+loxP]) II*	Maybe	Not tested	
NK2413	*sdn-1(qy29[sdn-1::mNG+loxP]) X.*	Yes	Yes	Uniform
NK2502	*ten-1(qy56[ten-1::mNG+loxP]) III*	No	No	
TH502	*unc-119(ed3) III; ddIs290[sax-7::TY1::EGFP::3xFLAG (92C12) + unc-119(+)].*	Yes	Yes	Uniform
NK2500	*unc-52(qy53[unc-52::mNG+loxP]) II*	No	Not tested	
NK2555	*unc-52(qy75[mNG+loxP::unc-52]) II*	Maybe	Yes	Uniform
NK2583	*unc-52(qy80[mNG+loxP (synthetic exon)::unc-52]) II*	Proximal PLM	Not tested	Patchy

FIGURE S1

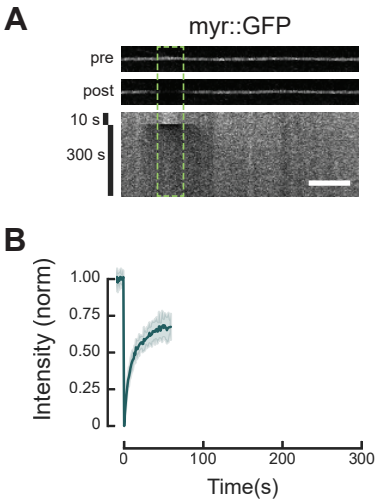
A
myr::GFP
pre
post
10 s
300 s
B
Intensity (norm)
1.00
0.75
0.50
0.25
0
0
100
200
300
Time(s)

FIGURE S2

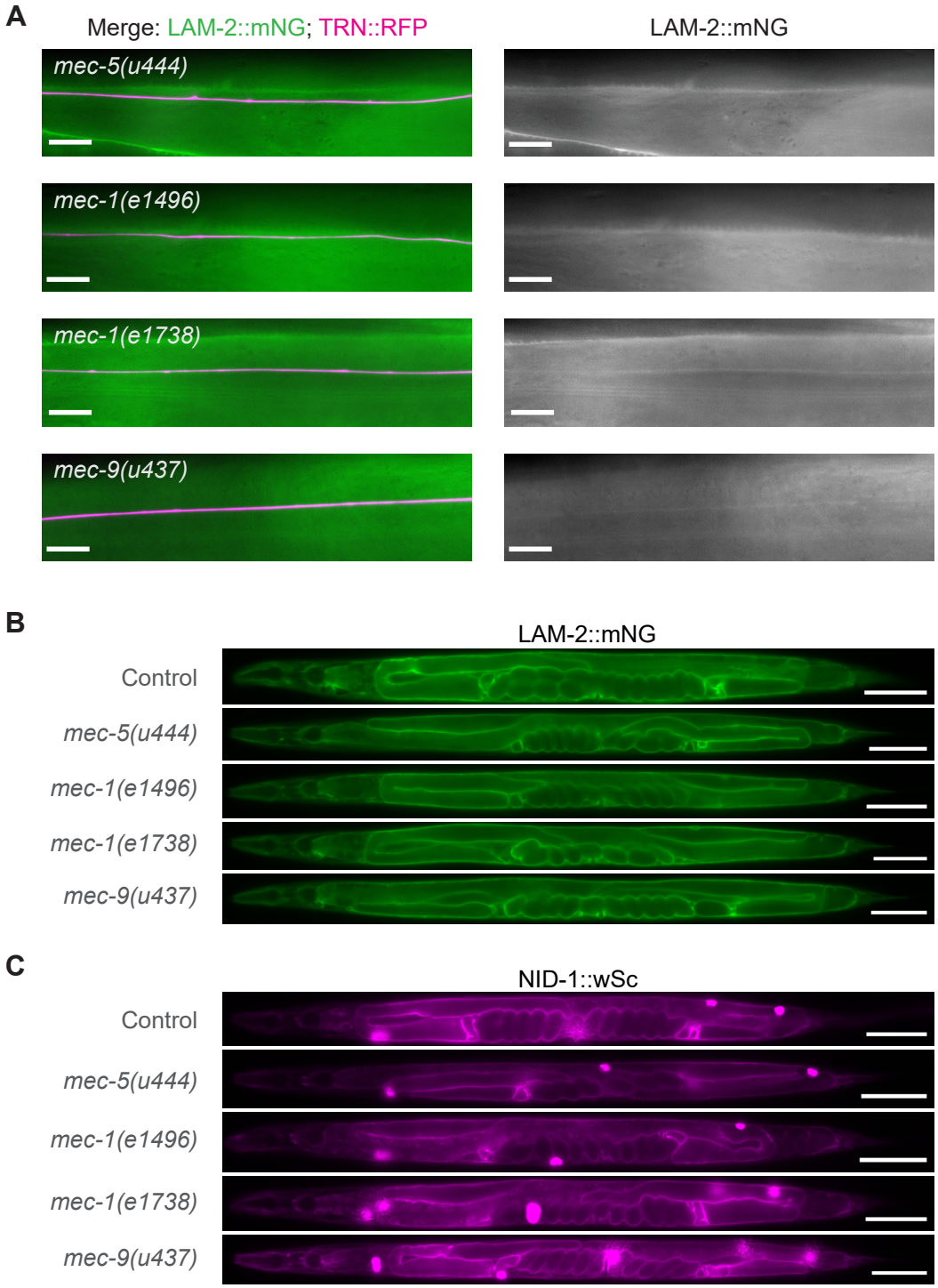
A
Merge: LAM-2::mNG; TRN::RFP
LAM-2::mNG
mec-5(u444)
mec-1(e1496)
mec-1(e1738)
mec-9(u437)
B
LAM-2::mNG
Control
mec-5(u444)
mec-1(e1496)
mec-1(e1738)
mec-9(u437)
C
NID-1::wSc
Control
mec-5(u444)
mec-1(e1496)
mec-1(e1738)
mec-9(u437)

FIGURE S3

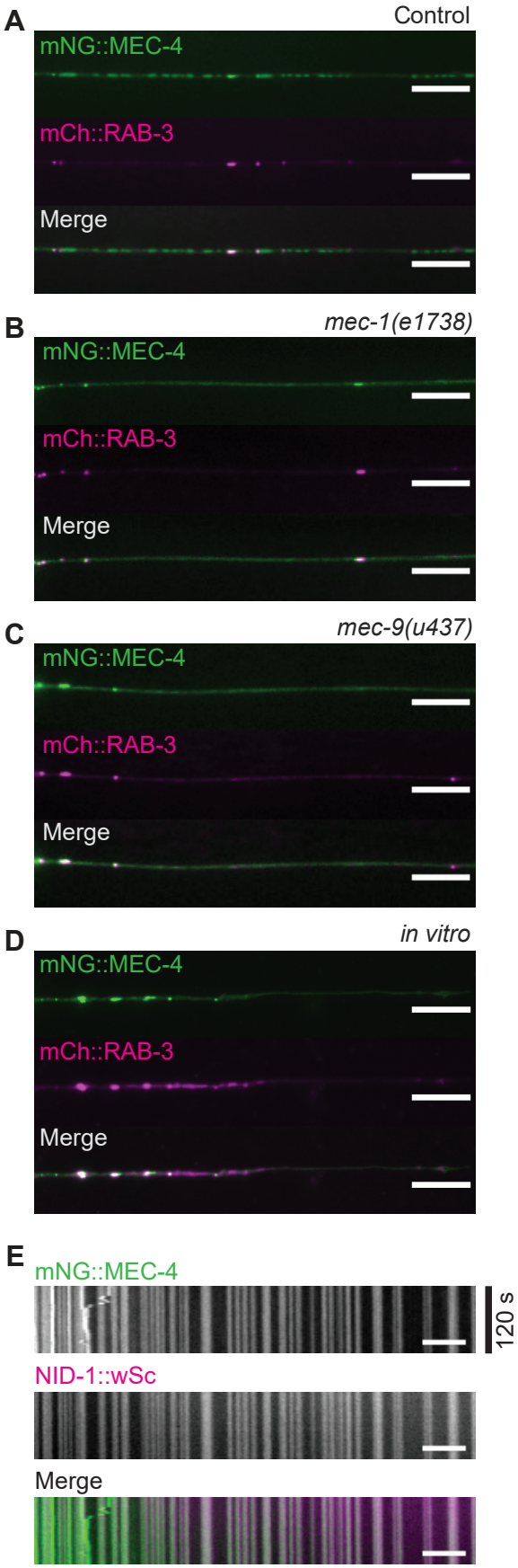
A
Control
mNG::MEC-4
mCh::RAB-3
Merge
B
mec-1(e1738)
mNG::MEC-4
mCh::RAB-3
Merge
C
mec-9(u437)
mNG::MEC-4
mCh::RAB-3
Merge
D
in vitro
mNG::MEC-4
mCh::RAB-3
Merge
E
mNG::MEC-4
120 s
NID-1::wSc
Merge

FIGURE S4

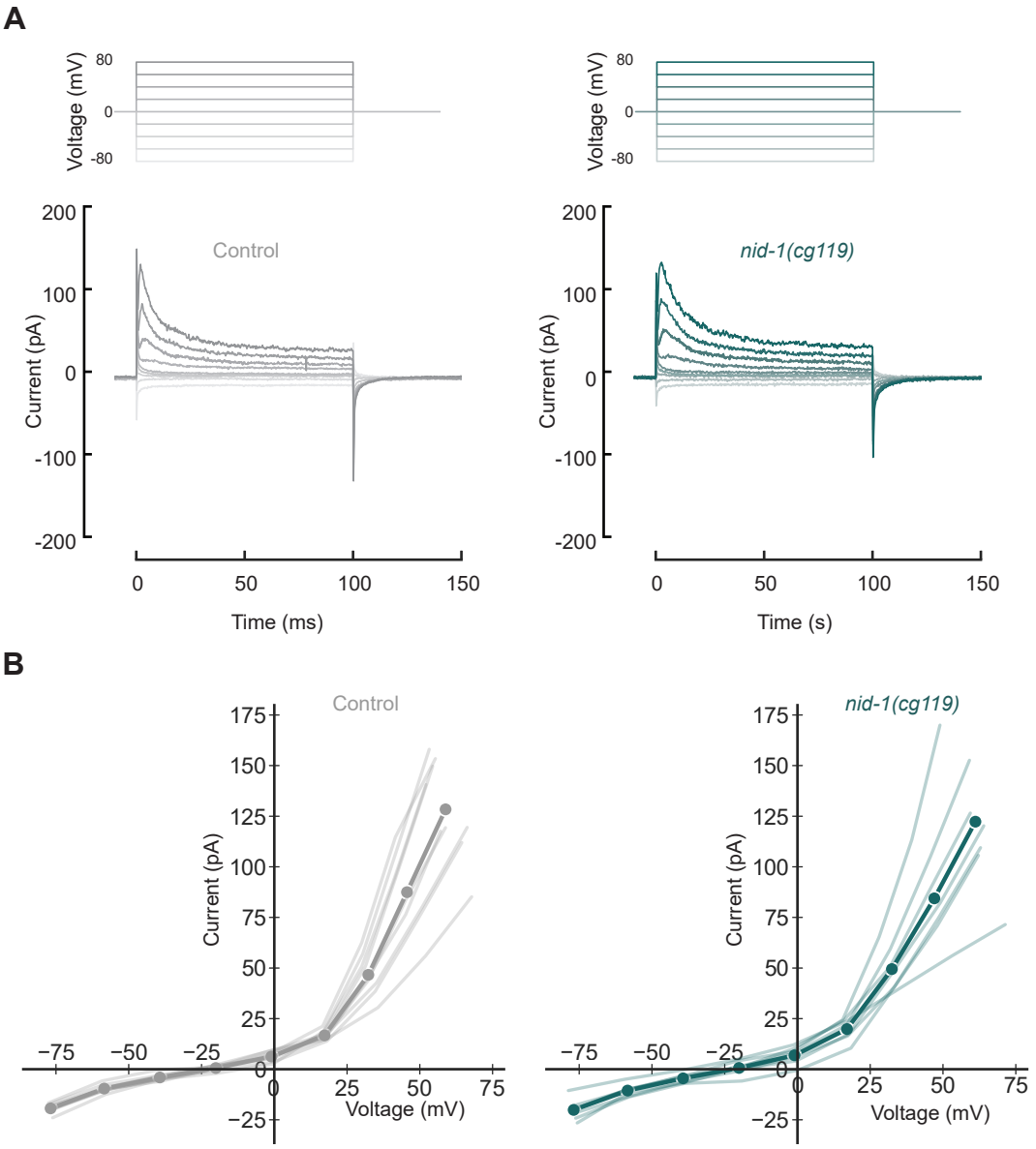
A
Voltage (mV)
80
0
-80
Control
nid-1(cg119)
Current (pA)
200
100
0
-100
-200
0
50
100
150
Time (ms)
Time (s)
B
Control
nid-1(cg119)
Current (pA)
175
150
125
100
75
50
25
0
−25
−75
−50
−25
0
25
50
75
Voltage (mV)

FIGURE S5

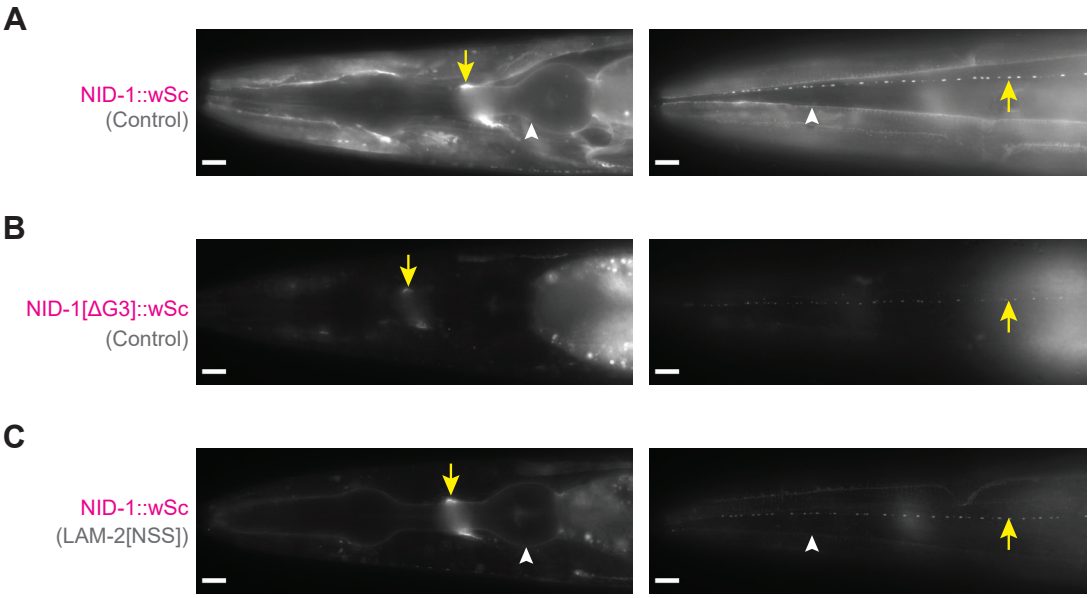

FIGURE S6

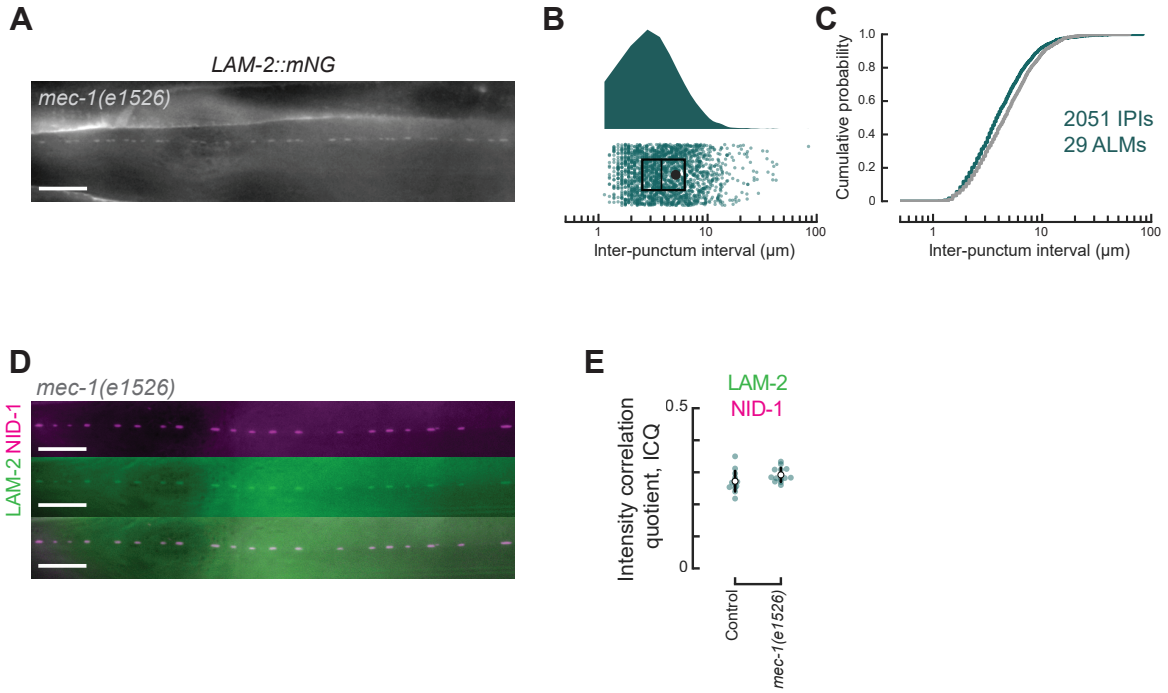
A
LAM-2::mNG
mec-1(e1526)
B
1
10
100
Inter-punctum interval (μm)
C
Cumulative probability
1.0
0.8
0.6
0.4
0.2
0
2051 IPIs
29 ALMs
1
10
100
Inter-punctum interval (μm)
D
mec-1(e1526)
LAM-2 NID-1
E
LAM-2
NID-1
Intensity correlation quotient, ICQ
0.5
0
Control
mec-1(e1526)